Turkish Journal of Electrical Engineering & Computer Sciences

http://journals.tubitak.gov.tr/elektrik/

Research Article

Turk J Elec Eng & Comp Sci
(2017) 25: 913 – 938

doi:10.3906/elk-1506-38

A self-tuning NeuroFuzzy feedback linearization-based damping control strategy for multiple HVDC links

Saghir AHMAD, Laiq KHAN*
Department of Electrical Engineering, COMSATS Institute of Information Technology, Abbottabad, Pakistan

Received: 04.06.2015 • **Accepted/Published Online:** 10.03.2016 • **Final Version:** 10.04.2017

Abstract: This research work proposes a multi-input multi-output (MIMO) online adaptive feedback linearization NeuroFuzzy control (AFLNFC) scheme to improve the damping of low frequency oscillations (LFOs) in an AC/DC power system. Optimized NeuroFuzzy identification architecture online captures the oscillatory dynamics of the power system through wide area measurement system (WAMS)-based measured speed signals of machines. Based on the identified power system model, the appropriate control law is derived through feedback linearization control with a self-tuned coefficient vector. The generated control signal modulates the real power flow through a high voltage direct current (HVDC) link during perturbed operating conditions and enhances system stability. The effectiveness of the proposed control strategy is demonstrated through different contingency conditions of a multi-machine test power system with multiple HVDC links. The results validate the significance of the proposed control strategy to improve the capability of HVDC links to damp inter-area modes of LFOs. The proposed MIMO AFLNFC performance is bench-marked against conventional PID based supplementary control.

Key words: Inter-area oscillation, high voltage direct transmission, adaptive NeuroFuzzy system, feedback linearization, nonlinear control

1. Introduction

High-efficiency operation and reliability of today's large interconnected power system are being considered more than ever. Increasing power demand and implementation of deregulation policies have led to increased interconnectivity, complexity, and uncertainties. This situation has resulted in a highly stressed transmission grid and power system stability, even in normal operating conditions, is critical. The operation of the power system is hindered considerably in the presence of low frequency electro-mechanical oscillations and may lead to cascading outages. To avoid the interruption of daily life and huge economic loss due to blackouts, it becomes imperative to ensure the damping of LFOs with time and augment dynamic stability [1].

Among all the possible available ways, one of the most prominent solutions is the better utilization of the existing power system through the controllability provided by high voltage DC (HVDC) transmission and flexible AC transmission systems (FACTS). Due to technical and economic advantages, the frequent applications of HVDC transmission system are rapidly increasing. HVDC operation involves no inertia and so rapid control of power flow is possible. The modulation of active power flow can be exploited to improve power system stability [2]. The majority of the HVDC systems in operation today are based on classic line-commutated

*Correspondence: laiq@ciit.net.pk

converters (LCCs) due to their high rating capability, lower power losses, better response to DC system faults, and simple configuration [3].

In the past, most researchers have focused on controlling a single HVDC link [4–6] as opposed to multiple HVDC links [7–9]. Approaches based on the approximate linearized model close to the specific operating point are adequate in a small range of operating conditions, but their performance deteriorates with variation in operating conditions over a wide range [10]. Commonly used robust control lacks learning ability and requires a priori known upper bounds on the uncertainties and suffers performance loss due to the wide ranging and increasing uncertainties of the power system [11]. A differential geometric theory-based feedback linearization technique can be a better choice to design the nonlinear control system. However, its application is quite limited due to dependence on the exact knowledge of the system nonlinearities. To confront this problem, an adaptive feedback linearizing control scheme is applied to nonlinear systems with unknown or uncertain parameters. Feedback linearization control with constant coefficients suffers performance loss under a wide range of operating conditions and can be improved through online tuning of controller coefficients [12].

In [13], feedback linearization control (FLC) with neural network architecture is used to implement a FACTS damping controller. Neural networks have learning ability, but they are prone to overfitting, have an opaque nature, and require a sufficient amount of the data of a problem for its training [14]. Hybridization of neural networks and fuzzy logic is an attempt to tackle these drawbacks of neural networks. NeuroFuzzy techniques integrate the benefits of a simple and natural structured fuzzy logic system, enabling the inclusion of linguistic knowledge into neural networks, which have learning capability [15]. An adaptive NeuroFuzzy controller acquires capabilities of parallel processing, faster learning, and better adaptation and approximation [16]. Furthermore, real-time instantaneous parameter adaptation has a fast response that enables rapid adjustment of parameters as compared to batch mode processing [17].

The above discussion motivates us to propose a MIMO AFLNFC scheme for modulation of power flow through HVDC links to improve the damping of LFOs. In the proposed MIMO AFLNFC framework, adaptive NeuroFuzzy architecture is optimized for real-time identification of system dynamics and the controller parameters are adjusted based on the identified model. For a wide ranging operating condition, the self-tuning capability of FLC tracks the power system output to handle uncertainties. Features of real-time online adaptive NeuroFuzzy identification and self-tuning of FLC coefficients make the proposed MIMO AFLNFC suitable for real-time control of MIMO nonlinear system quickly reacting under external disturbances. A case study of a multi-area test power system with two HVDC links demonstrates that the adaptive NeuroFuzzy identification and self-tuned feedback linearization control depicts better closed-loop response with improved post-disturbance stability in comparison with convention PID control. The main contributions of this research include:

- Modeling of the multi-machine power system with two HVDC links installed for bulk power transmission.
- Design of self-tuned robust MIMO AFLNFC for multiple HVDC links to exploit their additive benefit of instantaneous power flow control for damping inter-area modes of LFOs.
- Online optimization of NeuroFuzzy architecture used for identification of a large interconnected AC/DC power system.

The rest of the paper is organized as follows. Power system modeling and HVDC system dynamics are described in section 2. Section 3 explains the closed-loop control system design. The test system is illustrated in section 4. The results are presented and discussed in section 5. Section 6 includes conclusions on the findings of this research work.

2. AC/DC power system model description

2.1. Power system model

A set of differential and algebraic equations describe the power system model for different power system components with their associated controls.

$$\dot{\chi} = f(\chi, \psi) \tag{1}$$

$$0 = g(\chi, \psi), \tag{2}$$

where χ is the vector of state variables, ψ contains the algebraic variables, f represents the nonlinear differential equations of synchronous machines and control dynamics, and g defines load flow and network algebraic equations. This research work uses a 6th order machine model represented in the rotor dq-reference frame for each generator of a multi-machine power system. The 6th order model of the ith synchronous machine is given by the following differential equations with notation consistent with [18]:

$$\frac{d\delta}{dt} = \omega_r - \omega_s = \Delta\omega_r \tag{3}$$

$$2H\frac{d\Delta\omega_r}{dt} = (P_m - P_e - D\Delta\omega_r) \tag{4}$$

$$T'_{qo}\frac{dE'_d}{dt} = \left(x_q - x'_q\right)\left\{I_q - \frac{x'_q - x''_q}{\left(x'_q - x_{lk,s}\right)^2}\left(\psi_{2q} + \left(x'_q - x_{lk,s}\right)I_q + E'_d\right)\right\} - E'_d \tag{5}$$

$$T'_{do}\frac{dE'_q}{dt} = -\left(x_d - x'_d\right)\left\{I_d - \frac{x'_d - x''_d}{\left(x'_d - x_{lk,s}\right)^2}\left(\psi_{1d} + \left(x'_d - x_{lk,s}\right)I_d - E'_q\right)\right\} - E'_q + E_{fd} \tag{6}$$

$$T''_{do}\frac{d\psi_{1d}}{dt} = -\psi_{1d} + E'_q - \left(x_d - x_{lk,s}\right)I_d \tag{7}$$

$$T''_{qo}\frac{d\psi_{2q}}{dt} = -\psi_{2d} + E'_d - \left(x_q - x_{lk,s}\right)I_q \tag{8}$$

Assuming the generator armature resistance is negligible, the stator voltage and machine output power are defined by the following algebraic equations:

$$E_d = \frac{x''_q - x_{lk,s}}{x'_q - x_{lk,s}}E'_d - \frac{x'_q - x''_q}{x'_q - x_{lk,s}}\psi_{2q} + x''_q I_q \tag{9}$$

$$E_q = \frac{x''_d - x_{lk,s}}{x'_d - x_{lk,s}}E'_q + \frac{x'_d - x''_d}{x'_d - x_{lk,s}}\psi_{1d} + x''_d I_d \tag{10}$$

$$E_t = \sqrt{E_d^2 + E_q^2}\ , \quad P_e = E_d I_d + E_q I_q \tag{11}$$

The power plant model includes a detailed nonlinear turbine model with the governor system and IEEE type 1 voltage regulator model combined with an exciter. The AC transmission line is implemented through a distributed parameter line model with lumped losses. Different load models are considered, including a dynamic, constant PQ, and constant impedance load model.

2.2. HVDC dynamics

Figure 1 shows the AC/DC power system installed with two HVDC links. In this research, classic LCC-HVDC links are implemented through the average model with a converter unit represented by an equivalent voltage source generating the bridge average DC voltage and AC source generating the fundamental component of

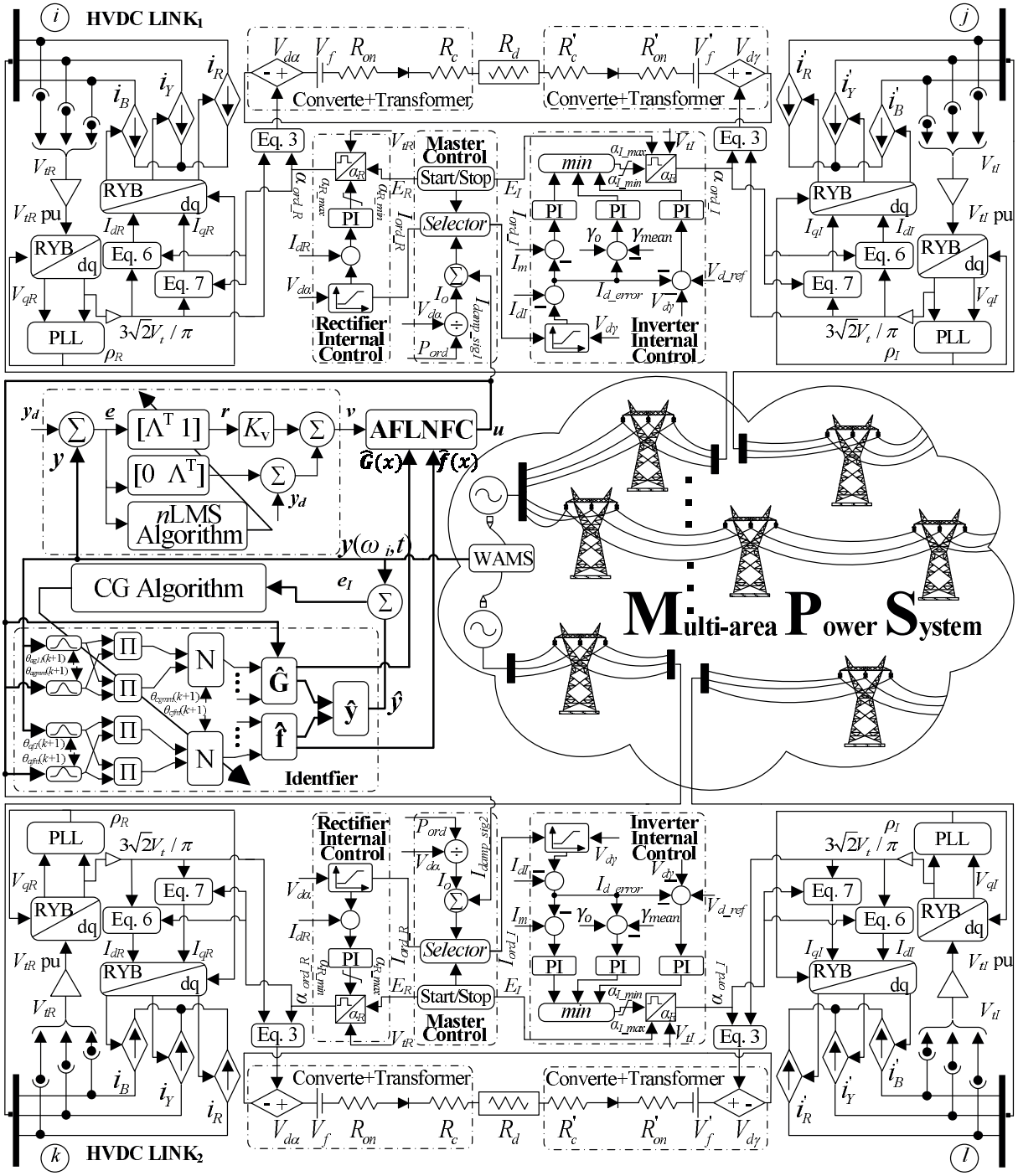

Figure 1. AC/DC power system model with two HVDC links.

current that flows into the AC network. The model does not represent high frequency switching harmonics, which are unnecessary for dynamic analysis and control dynamics. However, dynamics resulting from the control system and the power system interaction are preserved. Classic LCC-HVDC system provides active power flow control through a controllable parameter, the converter ignition angle α. Thus, average DC voltage is given as

$$V_d = \frac{6}{\pi}\int_{-\pi/6+\alpha}^{\pi/6+\alpha} \sqrt{2}aV_t \cos(\omega t)\, d(\omega t) = \frac{6\sqrt{2}}{\pi} aV_t \cos\alpha \tag{12}$$

Considering the reduction in voltage due to commutation overlap and effect of ignition delay, the average DC voltage at the rectifier and inverter is given as

$$V_{d\alpha} = V_{do\alpha}\cos\alpha - R_\alpha I_{d\alpha} \tag{13}$$

$$V_{d\gamma} = V_{do\gamma}\cos\gamma - R_\gamma I_{d\gamma}, \tag{14}$$

where $V_{do\alpha} = V_{do\gamma} = 6\sqrt{2}aV_t/\pi = V_{do}$ and $R_\alpha = R_\gamma = 6X_c/\pi = R_c$ is equivalent commutating resistance and accounts only for voltage drop due to the commutation overlap. The above equations show the inverter pole direct voltage as a function of γ, which is not directly controllable. The only direct controllable parameter at inverter pole is α and is related to γ as $\gamma = \pi - \alpha - \mu$. The injected current into the AC line is computed by the following relations in the dq-axis frame.

$$I_d = \frac{V_{do}(\cos 2\alpha - \cos(2\alpha + 2\mu))}{4\sqrt{6}aX_c} \tag{15}$$

$$I_q = -\frac{V_{do}(2\mu + \sin 2\alpha - \sin(2\alpha + 2\mu))}{4\sqrt{6}aX_c} \tag{16}$$

$$\mu = \cos^{-1}\left(\cos\alpha - \frac{2R_cI_d}{V_{do}}\right) - \alpha \tag{17}$$

A T-model for the DC line dynamics of LCC-HVDC system is utilized with DC voltage at both ends of the line [19]. With C_d, R_d, and L_d representing the capacitance, resistance, and inductance of the HVDC line, respectively, the following equations represent the dynamic model of the DC line:

$$L_d\frac{dI_{d\alpha}}{dt} = V_{d\alpha} - V_C - I_{d\alpha}R_d \tag{18}$$

$$L_d\frac{dI_{d\gamma}}{dt} = V_C - V_{d\gamma} - I_{d\gamma}R_d \tag{19}$$

$$C_d\frac{dV_C}{dt} = (I_{d\alpha} - I_{d\gamma}), \tag{20}$$

where V_C is the voltage across the line to ground capacitance of the DC line. If converter and transformer losses are ignored, then at each converter active power exchange between the AC and DC system is $P = V_dI_d$. As classic LLC-HVDC does not provide independent control of active and reactive powers, the corresponding reactive power absorbed by the converter is $Q = P\tan\vartheta$, where ϑ is the lagging phase difference between line-to-neutral source voltage and fundamental line current. For rectifier and inverter poles, ϑ is defined as

$$\vartheta_\alpha = \cos^{-1}\left(\cos\alpha - \frac{X_cI_{d\alpha}}{\sqrt{2}aV_{tR}}\right),\ \ \vartheta_\gamma = \cos^{-1}\left(\cos\gamma - \frac{X_cI_{d\gamma}}{\sqrt{2}aV_{tI}}\right) \tag{21}$$

2.3. LCC-HVDC control

High controllability is the key feature of the HVDC system and its appropriate application ensures the desired operation of the power system. The DC voltage at any point on the DC transmission line and current can be controlled through the gate control of the valve ignition angle or control of AC commutating voltage through tap changing. Rapid control action is accomplished through fast gate control followed by tap changing control to reinstate the firing delay angle and extinction advance angle within their normal range. To avoid unwanted variations in direct current over a wide range due to changes in AC voltage, fast converter control is essential for proper operation of the system.

The control architecture of a classic HVDC system is implemented by conventional PI controls. The same current order, I_{ord}, from master control is transmitted to the rectifier and inverter control that generate respective desired ignition angles α_{ord_R} and α_{ord_I}.

The current order is calculated as

$$I_{ord} = \frac{P_{\circ}}{V_{d\alpha}} + I_{damp\_sig} \tag{22}$$

During normal operation, current order is determined on the basis of power order and damping signal I_{damp_sig} is zero. Under perturbed operating conditions, external supplementary control generates I_{damp_sig}, which modifies the current order and hence the power flow through the HVDC link is modulated to improve the stability.

The rectifier, operated in constant current (CC) control mode, maintains a constant current with current reference subject to a voltage dependent current order limiter (VDCOL).

Considering α_{ord_R} and I_{dR} as the state variables, the rectifier current control is represented by

$$\dot{\alpha}_{ord\_R} = -K_{p\_R}\dot{I}_{dR} + K_{i\_R}(I_{ord} - I_{dR}) \tag{23}$$

The inverter operates in constant extinction angle control mode and aims to maintain the DC system voltage. Dynamics of inverter gamma control are given as

$$\dot{\alpha}_{ord\_I} = -K_{p\_I}\dot{\gamma} + K_{i\_I}(\gamma_{ref} - \gamma) \tag{24}$$

During the reduced commutating voltage, the inverter control switches to CC mode and a rectifier to constant ignition angle control mode with ignition delay angle $\alpha = \alpha_{\min}$. Moreover, in the case of low AC voltage, VDCOL defines the reduced current order depending upon the reduced DC voltage once it becomes less than the predefined threshold. Another feature of the inverter control is to provide current support for the situation when the DC current drops below a threshold equal to $I_{ord} - I_m$, where I_m is the current margin. Furthermore, α at the inverter is maintained in such a way that the extinction angle, γ, is not less than $\gamma_{\min}$ to ensure full extinction of valves and avoid commutation failures.

2.4. AC/DC interconnection

The HVDC converter is modeled as a current source generating the fundamental component of current that flows into the network. From Figure 2, the following equations are derived:

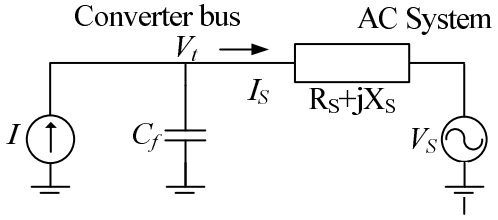

Figure 2. AC/DC interconnection.

$$C_f \frac{dV_t}{dt} = i - i_s \tag{25}$$

$$L_S \frac{di_S}{dt} = V_t - R_S i_S - V_S \tag{26}$$

Using dq-transformation, the following equations represent the model of AC/DC interconnection:

$$C_f \dot{v}_{td} = (i_d - i_{Sd}) + \dot{\theta} V_{tq} \tag{27}$$

$$C_f \dot{v}_{tq} = (i_q - i_{Sq}) + \dot{\theta} V_{td} \tag{28}$$

$$L_S \dot{i}_{Sd} = V_{td} - R_S i_{Sd} - V_{Sd} + \dot{\theta} i_{Sq} \tag{29}$$

$$L_S \dot{i}_{Sq} = V_{tq} - R_S i_{Sq} - V_{Sq} + \dot{\theta} i_{Sd} \tag{30}$$

where θ is a synchronously rotating reference frame.

3. Closed-loop control system design

The closed-loop control structure shown in Figure 1 is based on the model-free indirect adaptive control strategy requiring minimal knowledge of the plant. The proposed AFLNFC comprises the adaptive NeuroFuzzy identifier (ANFI) and feedback linearization control (FLC). The AC/DC power system model is identified through ANFI using WAMS-based measured actual speed signals of synchronous machines. The ANFI parameters are online optimized at each time step through the conjugate gradient (CG) algorithm to minimize the identification error. Based on the identified power system model, FLC generates an appropriate damping signal. The parameters of FLC are tuned online through the nLMS algorithm to maintain its performance over a wide range of operating conditions.

The following section explains the operation of ANFI, its parameters adaptation through the CG algorithm, and tuning of FLC coefficients.

3.1. Feedback linearization control

Feedback linearization is a nonlinear algebraic transformation that maps the nonlinear model into a linear one using feedback so that linear control techniques can be applied while preserving the nature of nonlinearities [20,21]. The nth order MIMO nonlinear system expressed in companion form or controllability canonical form is given as

$$\mathbf{y}^n = \mathbf{f}(\mathbf{x}) + \mathbf{G}(\mathbf{x})\mathbf{u} \tag{31}$$

where $\mathbf{u} \in \Re^m$ and $\mathbf{y} \in \Re^m$ are the input and output vectors of the MIMO nonlinear system, respectively. It is a square system with as many control inputs as outputs to be controlled. $\mathbf{x} \in \Re^{mn}$ is the state vector and $\mathbf{f}(x) \in \Re^m$ and $\mathbf{G}(x) \in \Re^{m \times m}$ represent smooth nonlinearities of the dynamic system.

Assumption 1 *As the nonlinear MIMO system is controllable,* $\mathbf{G}(x) \in \Re^{m \times m}$ *is invertible for all* $x \in U_c \subset \Re^{mn}$

If the MIMO nonlinear system input is expressed in terms of new input $\mathbf{v} \in \Re^n$, then the control law is defined as

$$\mathbf{u} = \mathbf{G}(\mathbf{x})^{-1} \left[-\mathbf{f}(\mathbf{x}) + \mathbf{v} \right] \tag{32}$$

The above control law will linearize the MIMO nonlinear system by cancelling the nonlinear terms. The input–output relation so obtained is of the form

$$\mathbf{y}^n = \mathbf{v} \tag{33}$$

However, functions $\mathbf{f}(\mathbf{x})$ and $\mathbf{G}(\mathbf{x})$ should be known to linearize the system. In this research work, the adaptive NeuroFuzzy architecture is employed to identify the nonlinear dynamics of the MIMO system and is explained in the following section.

3.2. Adaptive NeuroFuzzy identification

As shown in Figure 3, identification architecture is implemented with $m^2 + m$ NeuroFuzzy subsystem blocks. The jth rule for the NeuroFuzzy system identifying $f_\tau(x)$ and $g_{\tau h}(x)$, respectively, is of the form

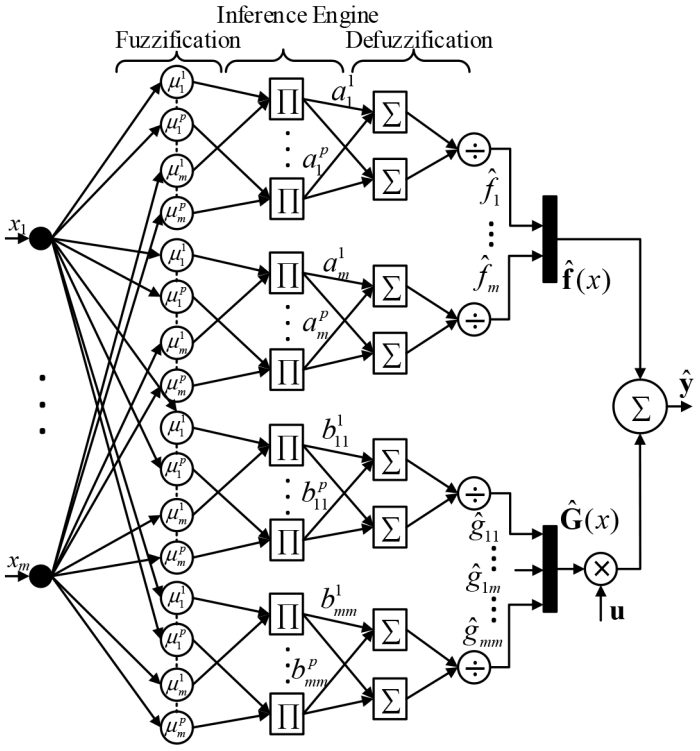

Figure 3. MIMO NeuroFuzzy identifier architecture.

Rule j: **If** x_1 is $F_{\tau 1}^j$ and x_2 is $F_{\tau 2}^j$ and $\cdots$ and x_m is $F_{\tau m}^j$, **Then** $\hat{f}_\tau$ is a_τ^j

$$\textbf{Rule } j\textbf{: If } x_1 \text{ is } G^j_{\tau h1} \text{ and } x_2 \text{ is } G^j_{\tau h2} \text{ and } \cdots \text{ and } x_m \text{ is } G^j_{\tau km}\textbf{, Then } \hat{g}_{\tau h} \text{ is } b^j_{\tau h},$$

where $F^j_{\tau i}$ and $G^j_{\tau hi}$ represent fuzzy sets of the antecedent part for the ith input and jth rule with $i, h, \tau = 1, 2, \cdots, m$ and $j = 1, 2, \cdots, p$. The network is implemented with Gaussian membership functions in the antecedent part, a product inference engine, and singleton variables in the consequent part. The whole network works in a layer fashion with layer 1 directly transmitting the input values to the next membership function layer. The adaptive nodes of layer 2 represent the Gaussian membership functions and are defined in generalized form as

$$\mu^j_i = \exp\left(-\frac{1}{2}\left(\frac{x_i - c^j_i}{\sigma^j_i}\right)^2\right), \tag{34}$$

where c^j_i is the center and σ^j_i is variance of the Gaussian membership function of the jth rule of the ith input. Layer 3 represents the IF-part of a fuzzy rule and calculates the firing strength of each rule using product T-norm, the generalized premise value of the jth rule in the rule base given as

$$\mu^j = \prod_{i=1}^{n} \mu^j_i(x_i) \tag{35}$$

A node in layer 4 represents the possible THEN-part of fuzzy rules and is adaptive. The links between nodes represent the consequences of the rule, i.e. a^j_τ and $b^j_{\tau h}$. The output variable of each NeuroFuzzy subsystem is represented by layer 5. The defuzzified crisp output computed by the node in this layer is identified as $\hat{f}_\tau(x)$ and $\hat{g}_{\tau h}(x)$ and given as

$$\hat{f}_\tau = \frac{\sum_{j=1}^{p} a^j_\tau \mu^j}{\sum_{j=1}^{p} \mu^j} = \sum_{j=1}^{p} \xi_j a^j_\tau \tag{36}$$

$$\hat{g}_{\tau h} = \frac{\sum_{j=1}^{p} b^j_{\tau h} \mu^j}{\sum_{j=1}^{p} \mu^j} = \sum_{j=1}^{p} \xi_j b^j_{\tau h}, \tag{37}$$

where $\xi_j = \frac{\mu_j}{\sum_{j=1}^{p} \mu_j}$ is the jth fuzzy basis function. The MIMO nonlinear system is identified as

$$\hat{\mathbf{y}} = \hat{\mathbf{f}}(\mathbf{x}) + \hat{\mathbf{G}}(\mathbf{x})\mathbf{u}, \tag{38}$$

where $\hat{\mathbf{f}}(\mathbf{x}) = \begin{bmatrix} \hat{f}_1(x) & \hat{f}_2(x) & \cdots & \hat{f}_m(x) \end{bmatrix}^T$ and $\hat{\mathbf{G}}(\mathbf{x}) = \begin{bmatrix} \hat{g}_{11}(x) & \cdots & \hat{g}_{1m}(x) \\ \vdots & \ddots & \vdots \\ \hat{g}_{m1}(x) & \cdots & \hat{g}_{mm}(x) \end{bmatrix}$

The identification error is defined as

$$\mathbf{e}_\tau(k) = \frac{1}{2}\varepsilon^T\varepsilon = \frac{1}{2}\left[\hat{\mathbf{y}}_\tau(k) - \mathbf{y}_\tau(k)\right]^2 \tag{39}$$

The objective is to minimize $\mathbf{e}_\tau(k)$ by optimization of parameters of ANFI architecture. The conjugate algorithm is employed to adapt the center and spread of the Gaussian membership function in the antecedent part and singleton functions in the consequent part.

3.2.1. Conjugate gradient algorithm for parameter adaptation

The conjugate gradient (CG) algorithm is characterized by low memory requirement with strong local and global convergence properties [22]. The nonlinear conjugate gradient method proposed in [23] provides sufficient descent independence of the line search. It reduces to a nonlinear version of Hestenes–Stiefel CG scheme for exact line search and satisfies the descent condition for any line search. It has been proved to be relatively robust in numerical computations. The CG algorithm-based parameter update law at $(k+1)th$ instant is defined as

$$\theta^{(k+1)} = \theta^{(k)} + \kappa_i \nu^{(k)}, \tag{40}$$

where $\kappa_i < 1$ is the learning rate for respective parameter, θ is the adaptation parameter, and $\nu^{(k)}$ is the conjugate search direction. The conjugate search is computed at each iteration as a linear combination of the current gradient of the function and previous search direction. At each instant its value is given as

$$\nu^{(k)} = \begin{cases} -\mathbf{d}^{(k)}, & k = 0 \\ -\mathbf{d}^{(k)} + \rho_k \nu^{(k-1)}, & k \geq 1 \end{cases} \tag{41}$$

Here $\mathbf{d}^{(k)} = \nabla f(\theta^{(k)})^T$, and ρ_k is a constant, chosen in such a way that new search direction, $\nu^{(k)}$, is orthogonal to the subspace generated by $\nu^{(\circ)}$, $\nu^{(1)}$, $\cdots$, $\nu^{(k-1)}$. According to [23], ρ_k is calculated as

$$\rho_k = \frac{1}{[\nu^{(k)}]^T \mathbf{s}^{(k)}} \left[\mathbf{s}^{(k)} - 2\nu^{(k)} \frac{\| \mathbf{s}^{(k)} \|^2}{[\nu^{(k)}]^T \mathbf{s}^{(k)}} \right]^T \mathbf{d}^{(k+1)}, \tag{42}$$

where $\mathbf{s}^{(k)} = \mathbf{d}^{(k+1)} - \mathbf{d}^{(k)}$.

Online CG algorithm for NeuroFuzzy parameter update is given in Algorithm 1.

Parameters of identification architectures are updated using the updated law of Eq. (40) based on minimization of the identification error defined in Eq. (39).

3.2.2. Parameter adaptation of consequent part

In each iteration of the CG algorithm, the error function gradient is to be calculated w.r.t. the respective consequent part parameter. The gradient of Eq. (39) using the chain rule of differentiation is given as

$$\begin{aligned} \frac{\partial e_\tau(k)}{\partial a_\tau^j} &= \frac{\partial e_\tau}{\partial \hat{y}_\tau} \frac{\partial \hat{y}_\tau}{\partial \hat{f}_\tau} \frac{\partial \hat{f}_\tau}{\partial a_\tau^j} = \varepsilon_\tau \xi_j \\ \frac{\partial e_\tau(k)}{\partial b_{\tau h}^j} &= \frac{\partial e_\tau}{\partial \hat{y}_\tau} \frac{\partial \hat{y}_\tau}{\partial \hat{g}_{\tau h}} \frac{\partial \hat{g}_{\tau h}}{\partial b_{\tau h}^j} = \varepsilon_\tau \xi_j u_\tau \end{aligned}, \tag{43}$$

where $\frac{\partial e_\tau}{\partial \hat{y}_\tau} = \varepsilon_\tau$, $\frac{\partial \hat{y}_\tau}{\partial \hat{f}_\tau} = 1$, $\frac{\partial \hat{y}_\tau}{\partial \hat{g}_\tau} = u_\tau$, $\frac{\partial \hat{f}_\tau}{\partial a_\tau^j} = \xi_j$, and $\frac{\partial \hat{g}_{\tau h}}{\partial b_{\tau h}^j} = \xi_j$. The jacobians of error function gradient w.r.t. a_τ and $b_{\tau h}$ are given as

$$J_{a_\tau} = \varepsilon_\tau \left[\begin{array}{cccc} \frac{\partial e_\tau(k)}{\partial a_\tau^1} & \frac{\partial e_\tau(k)}{\partial a_\tau^2} & \cdots & \frac{\partial e_\tau(k)}{\partial a_\tau^p} \end{array} \right]^T = \varepsilon_\tau \left[\begin{array}{cccc} \xi_1 & \xi_2 & \cdots & \xi_p \end{array} \right]^T \tag{44}$$

$$J_{b_{\tau h}} = \varepsilon_\tau \left[\begin{array}{cccc} \frac{\partial e_\tau(k)}{\partial b_{\tau h}^1} & \frac{\partial e_\tau(k)}{\partial b_{\tau h}^2} & \cdots & \frac{\partial e_\tau(k)}{\partial b_{\tau h}^p} \end{array} \right]^T u_\tau = \varepsilon_\tau \left[\begin{array}{cccc} \xi_1 & \xi_2 & \cdots & \xi_p \end{array} \right]^T u_\tau \tag{45}$$

Consequent parameters a_τ^j and $b_{\tau h}^j$ are updated through algorithm 3.2.1 using J_{a_τ} and $J_{b_{\tau h}}$ from Eqs. (44) and (45) with respective learning rates κ_{a_τ} and $\kappa_{b_{\tau h}}$.

Algorithm 1 Conjugate gradient algorithm for NeuroFuzzy parameter update

Given: Objective function, minimize error, $\mathbf{e}_\tau(k) = \frac{1}{2}\varepsilon^T\varepsilon = \frac{1}{2}\left[\hat{\mathbf{y}}_\tau(k) - \mathbf{y}_\tau(k)\right]^2$ through adaptation of parameters $\theta(\theta_{f_\tau}, \theta_{g_\tau h})$

- Learning rate, $\kappa_i > 0$
- Initialization, θ°

1. $k := 0$;
   (a) $\mathbf{d}^{(0)} = \nabla f(\theta^{(0)})^T = \frac{\partial e_\tau}{\partial \theta}|_{\theta=\theta^0}$;
   (b) $\mathbf{d}^0 = 0$;
   (c) Converged; stop.
2. Not converged
   (a) $\nu^0 = -\mathbf{d}^0$;
   (b) $\theta^{(k+1)} = \theta^{(k)} + \kappa\nu^{(k)}$;
   (c) $\mathbf{d}^{(k)} = \nabla f(\theta^{(k)}) = \frac{\partial e_\tau}{\partial \theta}|_{\theta=\theta^{(k)}}$;
   (d) $\mathbf{d}^{(k)} = 0$;
   (e) Converged; stop.
3. Not converged
   (a) $\rho_k = \frac{1}{[\nu^{(k)}]^T\mathbf{s}^{(k)}}\left[\mathbf{s}^{(k)} - 2\nu^{(k)}\frac{\|\mathbf{s}^{(k)}\|^2}{[\nu^{(k)}]^T\mathbf{s}^{(k)}}\right]^T\mathbf{d}^{(k+1)}$;
   (b) $\nu^{(k)} = -\mathbf{d}^{(k)} + \rho_k\nu^{(k-1)}$;
4. $k := k + 1$ return (2b)

3.2.3. Parameter adaptation of antecedent part

The gradient of error function w.r.t. the center and spread of the Gaussian membership function for identification of $\hat{f}_\tau$ is calculated as

$$\frac{\partial e_\tau(k)}{\partial c_{i\tau}^j} = \frac{\partial e_\tau(k)}{\partial \hat{y}_\tau}\frac{\partial \hat{y}_\tau}{\partial \hat{f}_\tau}\frac{\partial \hat{f}_\tau}{\partial \mu_{i\tau}^j}\frac{\partial \mu_{i\tau}^j}{\partial c_{i\tau}^j} = \varepsilon_\tau\left(\frac{a_\tau^j - \hat{f}_\tau}{\sum_j \mu_\tau^j}\right)\mu_\tau^j\left(\frac{x_i - c_{i\tau}^j}{(\sigma_{i\tau}^j)^2}\right) \tag{46}$$

$$\frac{\partial e_\tau(k)}{\partial \sigma_{i\tau}^j} = \frac{\partial e_\tau(k)}{\partial \hat{y}_\tau}\frac{\partial \hat{y}_\tau}{\partial \hat{f}_\tau}\frac{\partial \hat{f}_\tau}{\partial \mu_{i\tau}^j}\frac{\partial \mu_{\tau i}^j}{\partial \sigma_{i\tau}^j} = \varepsilon_\tau\left(\frac{a_{i\tau}^j - \partial\hat{f}_\tau}{\sum_j \mu_\tau^j}\right)\mu_\tau^j\left(\frac{(x_i - c_{i\tau}^j)^2}{(\sigma_{i\tau}^j)^3}\right) \tag{47}$$

and similarly for identification of $\hat{g}_{\tau h}$

$$\frac{\partial e_\tau(k)}{\partial c^j_{i\tau h}} = \frac{\partial e_\tau(k)}{\partial \hat{y}_\tau}\frac{\partial \hat{y}_\tau}{\partial \hat{g}_{\tau h}}\frac{\partial \hat{g}_{\tau h}}{\partial \mu^j_{i\tau h}}\frac{\partial \mu^j_{i\tau h}}{\partial c^j_{i\tau h}} = \varepsilon_\tau \left(\frac{a^j_{\tau h} - \hat{g}_{\tau h}}{\sum_j \mu^j_{\tau h}}\right)\mu^j_{i\tau}\left(\frac{x_i - c^j_{i\tau h}}{(\sigma^j_{i\tau h})^2}\right)u_\tau \tag{48}$$

$$\frac{\partial e_\tau(k)}{\partial \sigma^j_{i\tau h}} = \frac{\partial e_\tau(k)}{\partial \hat{y}_\tau}\frac{\partial \hat{y}_\tau}{\partial \hat{g}_{\tau h}}\frac{\partial \hat{g}_{\tau h}}{\partial \mu^j_{i\tau h}}\frac{\partial \mu^j_{i\tau h}}{\partial \sigma^j_{i\tau h}} = \varepsilon_\tau \left(\frac{a^j_{\tau h} - \hat{g}_{\tau h}}{\sum_j \mu^j_{\tau h}}\right)\mu^j_{\tau h}\left(\frac{(x_i - c^j_{i\tau h})^2}{(\sigma^j_{i\tau h})^3}\right)u_\tau \tag{49}$$

Using Eqs. (46) to (49), the jacobians of gradient of error function w.r.t. the center and spread of respective $\hat{f}_\tau$ and $\hat{g}_{\tau h}$ are given as

$$J_{c_{\hat{f}_\tau}} = \varepsilon_\tau \begin{bmatrix} \frac{(a^1_\tau - \hat{f}_\tau)(x_1 - c^1_{\tau 1})\mu^1_\tau}{(\sigma^1_{\tau 1})^2 \sum_j \mu^j_\tau} & \frac{(a^2_\tau - \hat{f}_\tau)(x_1 - c^2_{\tau 1})\mu^2_\tau}{(\sigma^2_{\tau 1})^2 \sum_j \mu^j_\tau} & \cdots & \frac{(a^p_\tau - \hat{f}_\tau)(x_1 - c^p_{\tau 1})\mu^p_\tau}{(\sigma^p_{\tau 1})^2 \sum_j \mu^j_\tau} \\ \frac{(a^1_\tau - \hat{f}_\tau)(x_2 - c^1_{\tau 2})\mu^1_\tau}{(\sigma^1_{\tau 2})^2 \sum_j \mu^j_\tau} & \frac{(a^2_\tau - \hat{f}_\tau)(x_2 - c^2_{\tau 2})\mu^2_\tau}{(\sigma^2_{\tau 2})^2 \sum_j \mu^j_\tau} & \cdots & \frac{(a^p_\tau - \hat{f}_\tau)(x_2 - c^p_{\tau 2})\mu^p_\tau}{(\sigma^p_{\tau 2})^2 \sum_j \mu^j_\tau} \\ \vdots & \vdots & \ddots & \vdots \\ \frac{(a^1_\tau - \hat{f}_\tau)(x_m - c^1_{\tau m})\mu^1_\tau}{(\sigma^1_{\tau m})^2 \sum_j \mu^j_\tau} & \frac{(a^2_\tau - \hat{f}_\tau)(x_m - c^2_{\tau m})\mu^2_\tau}{(\sigma^2_{\tau m})^2 \sum_j \mu^j_\tau} & \cdots & \frac{(a^p_\tau - \hat{f}_\tau)(x_m - c^p_{\tau m})\mu^p_\tau}{(\sigma^p_{\tau m})^2 \sum_j \mu^j_\tau} \end{bmatrix} \tag{50}$$

$$J_{\sigma_{\hat{f}_\tau}} = \varepsilon_\tau \begin{bmatrix} \frac{(a^1_\tau - \hat{f}_\tau)(x_1 - c^1_{\tau 1})^2\mu^1_\tau}{(\sigma^1_{\tau 1})^3 \sum_j \mu^j_\tau} & \frac{(a^2_\tau - \hat{f}_\tau)(x_1 - c^2_{\tau 1})^2\mu^2_\tau}{(\sigma^2_{\tau 1})^3 \sum_j \mu^j_\tau} & \cdots & \frac{(a^p_\tau - \hat{f}_\tau)(x_1 - c^p_{\tau 1})^2\mu^p_\tau}{(\sigma^p_{\tau 1})^3 \sum_j \mu^j_\tau} \\ \frac{(a^1_\tau - \hat{f}_\tau)(x_2 - c^1_{\tau 2})^2\mu^1_\tau}{(\sigma^1_{\tau 2})^3 \sum_j \mu^j_\tau} & \frac{(a^2_\tau - \hat{f}_\tau)(x_2 - c^2_{\tau 2})^2\mu^2_\tau}{(\sigma^2_{\tau 2})^3 \sum_j \mu^j_\tau} & \cdots & \frac{(a^p_\tau - \hat{f}_\tau)(x_2 - c^p_{\tau 2})^2\mu^p_\tau}{(\sigma^p_{\tau 2})^3 \sum_j \mu^j_\tau} \\ \vdots & \vdots & \ddots & \vdots \\ \frac{(a^1_\tau - \hat{f}_\tau)(x_m - c^1_{\tau m})^2\mu^1_\tau}{(\sigma^1_{\tau m})^3 \sum_j \mu^j_\tau} & \frac{(a^2_\tau - \hat{f}_\tau)(x_m - c^2_{\tau m})^2\mu^2_\tau}{(\sigma^2_{\tau m})^3 \sum_j \mu^j_\tau} & \cdots & \frac{(a^p_\tau - \hat{f}_\tau)(x_m - c^p_{\tau m})^2\mu^p_\tau}{(\sigma^p_{\tau m})^3 \sum_j \mu^j_\tau} \end{bmatrix} \tag{51}$$

$$J_{c_{\hat{g}_{\tau h}}} = \varepsilon_\tau \begin{bmatrix} \frac{(a^1_{\tau h} - \hat{g}_{\tau h})(x_1 - c^1_{\tau h1})\mu^1_{\tau h}}{(\sigma^1_{\tau h1})^2 \sum_j \mu^j_{\tau h}} & \frac{(a^2_{\tau h} - \hat{g}_{\tau h})(x_1 - c^2_{\tau h1})\mu^2_{\tau h}}{(\sigma^2_{\tau h1})^2 \sum_j \mu^j_{\tau h}} & \cdots & \frac{(a^p_{\tau h} - \hat{g}_{\tau h})(x_1 - c^p_{\tau h1})\mu^p_{\tau h}}{(\sigma^p_{\tau h1})^2 \sum_j \mu^j_{\tau h}} \\ \frac{(a^1_{\tau h} - \hat{g}_{\tau h})(x_2 - c^1_{\tau h2})\mu^1_{\tau h}}{(\sigma^1_{\tau h2})^2 \sum_j \mu^j_{\tau h}} & \frac{(a^2_{\tau h} - \hat{g}_{\tau h})(x_2 - c^2_{\tau h2})\mu^2_{\tau h}}{(\sigma^2_{\tau h2})^2 \sum_j \mu^j_{\tau h}} & \cdots & \frac{(a^p_{\tau h} - \hat{g}_{\tau h})(x_2 - c^p_{\tau h2})\mu^p_{\tau h}}{(\sigma^p_{\tau h2})^2 \sum_j \mu^j_{\tau h}} \\ \vdots & \vdots & \ddots & \vdots \\ \frac{(a^1_{\tau h} - \hat{g}_{\tau h})(x_m - c^1_{\tau hm})\mu^1_{\tau h}}{(\sigma^1_{\tau hm})^2 \sum_j \mu^j_{\tau h}} & \frac{(a^2_{\tau h} - \hat{g}_{\tau h})(x_m - c^2_{\tau hm})\mu^2_{\tau h}}{(\sigma^2_{\tau hm})^2 \sum_j \mu^j_{\tau h}} & \cdots & \frac{(a^p_{\tau h} - \hat{g}_{\tau h})(x_m - c^p_{\tau hm})\mu^p_{\tau h}}{(\sigma^p_{\tau hm})^2 \sum_j \mu^j_{\tau h}} \end{bmatrix} u_\tau \tag{52}$$

$$J_{\sigma_{\hat{g}_{\tau h}}} = \varepsilon_\tau \begin{bmatrix} \frac{(a^1_{\tau h} - \hat{g}_{\tau h})(x_1 - c^1_{\tau h1})^2\mu^1_{\tau h}}{(\sigma^1_{\tau h1})^3 \sum\limits_j \mu^j_{\tau h}} & \frac{(a^2_{\tau h} - \hat{g}_{\tau h})(x_1 - c^2_{\tau h1})^2\mu^2_{\tau h}}{(\sigma^2_{\tau h1})^3 \sum\limits_j \mu^j_{\tau h}} & \cdots & \frac{(a^p_{\tau h} - \hat{g}_{\tau h})(x_1 - c^p_{\tau h1})^2\mu^p_{\tau h}}{(\sigma^p_{\tau h1})^3 \sum\limits_j \mu^j_{\tau h}} \\ \frac{(a^1_{\tau h} - \hat{g}_{\tau h})(x_2 - c^1_{\tau h2})^2\mu^1_{\tau h}}{(\sigma^1_{\tau h2})^3 \sum\limits_j \mu^j_{\tau h}} & \frac{(a^2_{\tau h} - \hat{g}_{\tau h})(x_2 - c^2_{\tau h2})^2\mu^2_{\tau h}}{(\sigma^2_{\tau h2})^3 \sum\limits_j \mu^j_{\tau h}} & \cdots & \frac{(a^p_{\tau h} - \hat{g}_{\tau h})(x_2 - c^p_{\tau h2})^2\mu^p_{\tau h}}{(\sigma^p_{\tau h2})^3 \sum\limits_j \mu^j_{\tau h}} \\ \vdots & \vdots & \ddots & \vdots \\ \frac{(a^1_{\tau h} - \hat{g}_{\tau h})(x_m - c^1_{\tau hm})^2\mu^1_{\tau h}}{(\sigma^1_{\tau hm})^3 \sum\limits_j \mu^j_{\tau h}} & \frac{(a^2_{\tau h} - \hat{g}_{\tau h})(x_m - c^2_{\tau hm})^2\mu^2_{\tau h}}{(\sigma^2_{\tau hm})^3 \sum\limits_j \mu^j_{\tau h}} & \cdots & \frac{(a^p_{\tau h} - \hat{g}_{\tau h})(x_m - c^p_{\tau hm})^2\mu^p_{\tau h}}{(\sigma^p_{\tau hm})^3 \sum\limits_j \mu^j_{\tau h}} \end{bmatrix} u_\tau \tag{53}$$

Parameters of Gaussian membership function c_i^j and σ_i^j for identification of $\hat{f}_\tau$ and $\hat{g}_{\tau h}$ are updated through algorithm 3.2.1 using respective jacobians from Eqs. (50) to (53). The learning rates for antecedent parameters are κ_{f_τ} and $\kappa_{g_{\tau h}}$. The CG algorithm determines the appropriate parameters of the NeuroFuzzy system for real-time identification of nonlinear dynamics of the AC/DC power system to design a control law of Eq. (32).

3.2.4. Self-tuning feedback linearization control

For the system defined in Eq. (31), the MIMO AFLNFC objective is to define a control law $\mathbf{u} \in \Re^m$, such that the plant follows a desired signal $\mathbf{y}_d \in \Re^m$ with an acceptable accuracy, while all the states and controls remain bounded. The control law defined in Eq. (32) is based on the identified system model and input $\mathbf{v} \in \Re^m$.

Assumption 2 *The desired trajectory $\mathbf{y}_d(t)$ is continuous, bounded, and available for online control computation*

Assumption 3 ***Assumption 3*** *- There are no zero dynamics*

An error matrix $\mathbf{e} \in \Re^{n\times m}$ is defined as

$$x - x_d(t) = \begin{bmatrix} y_1 - y_{d_1} & y_2 - y_{d_2} & \cdots & y_m - y_{d_m} \\ \dot{y}_1 - \dot{y}_{d_1} & \dot{y}_2 - \dot{y}_{d_2} & \cdots & \dot{y}_m - \dot{y}_{d_m} \\ \vdots & \vdots & \vdots & \vdots \\ y_1^{(n-1)} - y_{d_1}^{(n-1)} & y_2^{(n-1)} - y_{d_2}^{(n-1)} & \cdots & y_m^{(n-1)} - y_{d_m}^{(n-1)} \end{bmatrix} \tag{54}$$

The product of error matrix and weight vectors defines the filter tracking error $\mathbf{r}$ and is given as

$$\mathbf{r}^T = \begin{bmatrix} \lambda_1 & \lambda_2 & \cdots & \lambda_{n-1} & 1 \end{bmatrix} \begin{bmatrix} y_1 - y_{d_1} & y_2 - y_{d_2} & \cdots & y_m - y_{d_m} \\ \dot{y}_1 - \dot{y}_{d_1} & \dot{y}_2 - \dot{y}_{d_2} & \cdots & \dot{y}_m - \dot{y}_{d_m} \\ \vdots & \vdots & \vdots & \vdots \\ y_1^{(n-1)} - y_{d_1}^{(n-1)} & y_2^{(n-1)} - y_{d_2}^{(n-1)} & \cdots & y_m^{(n-1)} - y_{d_m}^{(n-1)} \end{bmatrix} = \begin{bmatrix} \Lambda^T & 1 \end{bmatrix} \underline{e}, \tag{55}$$

where $\Lambda = \begin{bmatrix} \lambda_1 & \lambda_2 & \cdots & \lambda_{n-1} \end{bmatrix}$ are constants.

Remark 1 *Λ is appropriately chosen so that the poles of $s^{n-1} + \lambda_{n-1}s^{n-2} + \cdots + \lambda_1$ strictly lie in the left half of the complex plane.*

Taking the derivative of Eq. (55) and using Eq. (54), we have

$$\mathbf{r}^T = \begin{bmatrix} y_1^n \\ y_2^n \\ \vdots \\ y_m^n \end{bmatrix} + \begin{bmatrix} -y_{d_1}^n \\ -y_{d_2}^n \\ \vdots \\ -y_{d_m}^n \end{bmatrix} + \begin{bmatrix} 0 & \Lambda^T \end{bmatrix} e = \begin{bmatrix} y_1^n \\ y_2^n \\ \vdots \\ y_m^n \end{bmatrix} + \mathbf{Y}_D^T \quad \in \Re^{1\times m} \tag{56}$$

Using Eqs. (31) and (56), we have

$$\dot{\mathbf{r}} = \mathbf{y}^n + \mathbf{Y}_d = \mathbf{f}(x) + \mathbf{G}(\mathbf{x})\mathbf{u} + \mathbf{Y}_D \tag{57}$$

Using $\dot{\mathbf{r}} = -K_v\mathbf{r}$ in the above equation gives

$$-K_v\mathbf{r} = \mathbf{f}(\mathbf{x}) + \mathbf{G}(\mathbf{x})\mathbf{u} + \mathbf{Y}_D \tag{58}$$

If the functions, $\mathbf{f}(\mathbf{x})$ and $\mathbf{G}(\mathbf{x})$, are exactly known, the control law can be written as

$$\mathbf{u} = \mathbf{G}^{-1}(\mathbf{x})\left[-\mathbf{f}(\mathbf{x}) - K_v\mathbf{r} - \mathbf{Y}_D\right], \tag{59}$$

where $-K_v\mathbf{r} - \mathbf{Y}_D = \mathbf{v}$. For $K_v > 0$ this control law would bring r to zero. With estimated $\hat{\mathbf{f}}$ and $\hat{\mathbf{G}}$ through NeuroFuzzy identification and $\hat{\mathbf{G}}$ not singular, the control law would become

$$\mathbf{u} = \hat{\mathbf{G}}^{-1}(\mathbf{x})[-\widehat{\mathbf{f}}(\mathbf{x}) + \mathbf{v}] \tag{60}$$

An appropriate value of Λ will ensure that $s^{n-1} + \lambda_{n-1}s^{n-2} + \cdots + \lambda_1$ is stable. Under normal operating conditions, fixing Λ to an appropriate constant value will result in $e \to 0$ as $r \to 0$. However, during contingency situations with variable operating conditions, the performance of the controller will deteriorate with constant Λ and is required to be updated based on changes in operating conditions. The nLMS algorithm is applied to tune the coefficient vector, Λ, at each time step to achieve better performance of FLC.

3.3. Normalized least mean square algorithm for Λ adaptation

Eq. (55) is written as

$$\mathbf{r} = \varphi^T\Lambda + \rho, \tag{61}$$

where $\varphi^T = \begin{bmatrix} e & \dot{e} & \cdots & e^{(n-2)} \end{bmatrix}$ and $\rho = e^{(n-1)}$. With an estimation of Λ as $\hat{\Lambda}$, estimated filter tracking error at kth instant is

$$\mathbf{r}(k) = \varphi^T(k)\hat{\Lambda}(k) + \rho(k) \tag{62}$$

Updating of $\hat{\Lambda}$ can be written as the following minimization problem:

$$\begin{cases} \text{mimimize} & \left\|\hat{\Lambda}(k) - \hat{\Lambda}(k-1)\right\|_2^2 \\ \text{subject to} & \mathbf{r}(k) = \varphi(k)\hat{\Lambda}(k) + \rho(k) \end{cases}$$

Using Lagrangian multiplier β, the objective function becomes

$$E(\hat{\Lambda}(k), \hat{\Lambda}(k-1), k) = \frac{1}{2}\left\|\hat{\Lambda}(k) - \hat{\Lambda}(k-1)\right\|_2^2 + \beta\left(r(k) - \varphi^T(k)\hat{\Lambda}(k) - \rho(k)\right) \tag{63}$$

To generate an appropriate control signal, $\Lambda(k)$ is updated at each iteration using nLMS given by Algorithm 2.

3.4. Computational steps for closed-loop control system

After the discussion of individual components of CLCS, the following steps summarize the flow of the algorithm for damping LFOs in the AC/DC power system.

1. Actual speed signals, $\omega_1, \omega_2, \ldots, \omega_7$, of generators are measured through WAMS.

Algorithm 2 Normalized LMS algorithm for Λ adaptation

Step 1: *Initialization*

$$\hat{\Lambda}(k) = [\ \lambda_1 \quad \lambda_1 \quad \cdots \quad \lambda_{n-1}\ ], 0 < \gamma < 2 and \eta \geq 0$$

Step 2: *Do it for* $k \geq 0$

$$e(k) = x(k) - x_d(k) \text{ and } r = [\Lambda^T 1]e$$

$$\hat{\Lambda}(k) = \hat{\Lambda}(k-1) + \frac{\varphi(k)}{\varphi^T(k)\varphi(k)} \left\{ r(k) - \varphi(k)\hat{\Lambda}(k-1) - \rho(k) \right\}$$

2. Speed deviations of different machines are calculated as $y^T = [\ y_1 \quad y_2\ ]$, where $y_1 = \sum_{i=1}^{5} (\omega_1 - \omega_i)$ and $y_2 = \sum_{i=6}^{7} (\omega_1 - \omega_i)$.

3. Based on y_1 and y_2, ANFI captures the unknown nonlinear dynamics of the power system as defined in Eq. (38).

4. At each time step, the CG algorithm optimizes the parameters of ANFI through Algorithm 1 to minimize the identification error $y - \hat{y}$.

5. In parallel to steps 3 and 4, online estimation generates $\mathbf{v} \in \Re^n$ with the nLMS algorithm tuning the optimal value of the coefficients vector Λ that minimizes the estimation error $y - y_d$.

6. Based on identified functions $\hat{f}$ and $\hat{G}$, FLC with optimized coefficient vector generates an appropriate control law $u^T = [\ u_1 \quad u_2\ ]$ according to Eq. (60).

7. u_1 and u_2 are inputs to master control of HVDC$_1$ and HVDC$_2$ as I_{damp_sig1} and I_{damp_sig2}, respectively. These current signals modulate the reference current order according to Eq. (22) during perturbed operating conditions.

8. Rectifier and inverter control of each HVDC link generates respective α_{ord} according to I_{ord} as intimated by master control as shown in Figure 1.

9. Based on α_{ord}, each HVDC system sets its voltage and current and hence power flow through it as discussed in section 2.2.

10. During perturbed operating conditions, presence of energy in the power system varies the speed of generators and hence the speed deviations. Based on these variations, the rapid power flow control of the HVDC link by AFLNFC will minimize the effect of energy present in the power system and damp the power oscillations to improve power system stability.

4. Test system

The test system considered in this research work is a simplified model of the Hydro-Québec (HQ) system with the addition of two HVDC links as shown in Figure 4 [24]. The test system is implemented in SIMULINK/SimPowerSystem through nonlinear differential-algebraic equations. The AC/DC power system comprises North-West (NW) network and North-East (NE) network further distributed over seven different areas designated as $A\#1$ to $A\#7$.

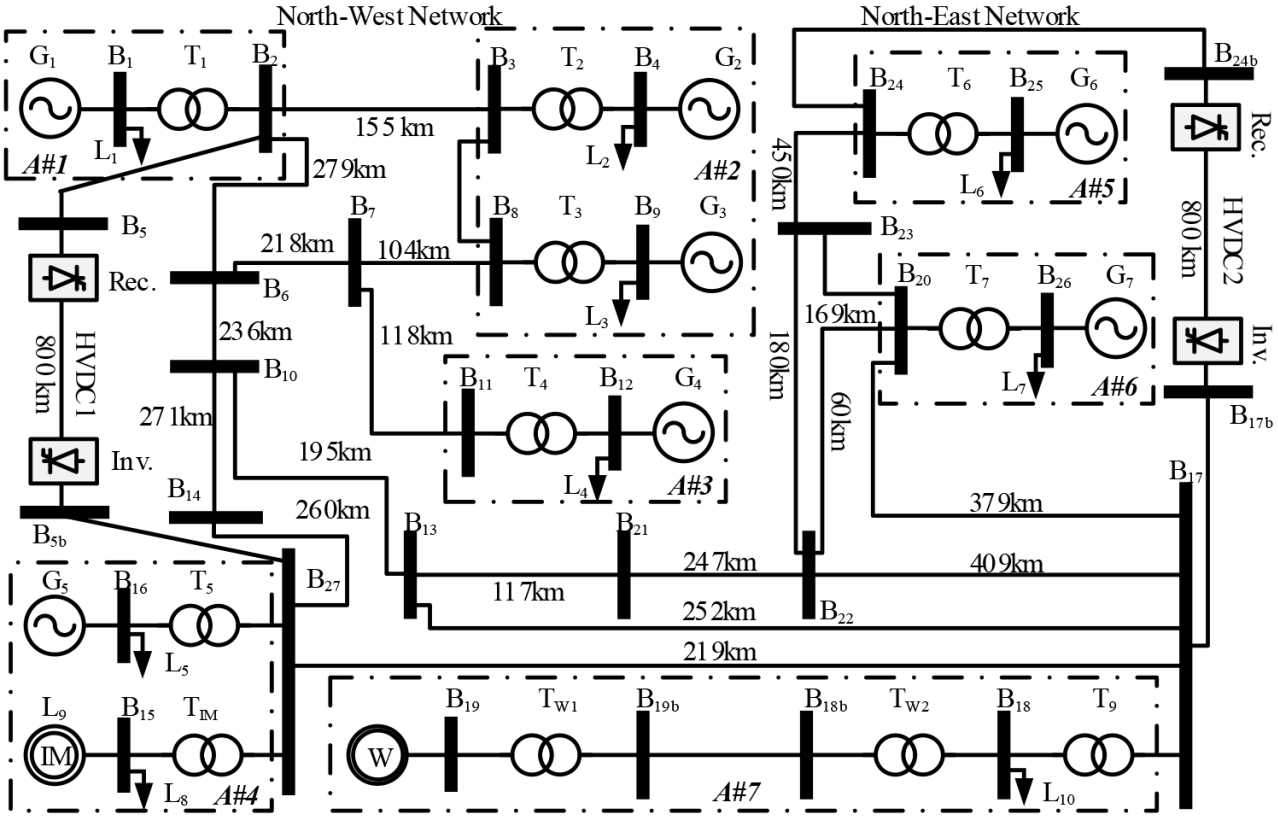

Figure 4. AC/DC multi-machine power system.

Seven 13.8 kV power plants (G_1 to G_7), with detailed models, including hydraulic turbines, speed regulation, and excitation systems, are located in different areas. Plants are connected through a huge 735 kV transmission network with fixed series and shunt compensation provided at key locations. Two networks are connected through tie-lines $B_{13}B_{22}$, $B_{13}B_{17}$, and $B_{29}B_{17}$.

The total generation capacity of the seven plants is 27,000 MW and connected load is 23,000 MW. Major load is lumped at two buses, B_{27} and B_{17}. The 15,500 MW load at bus B_{27} includes dynamic load, constant PQ, constant Z, and induction motor load at 25 kV, while bus B_{17} load consists of constant Z and constant PQ load of 6000 MW at 120 kV. Under nominal conditions, about 45% of load demand is exported to load centers from the NW network and 35% from the NE network. Bus B_{17} is fed by a wind farm producing 9 MW and is left uncontrolled to see the effect of HVDC link modulation.

To support large power transfer from remote power generation resources, two HVDC links are installed in the transmission network connecting buses B_2B_{27} and $B_{24}B_{17}$. Under steady-state conditions, each HVDC system delivers 1000 MW at 500 kV through the 800-km line. The converters are represented by average models of 12-pulse converters representing two 6-pulse series connected thyristor bridges. Control signals I_{damp_sig1} and I_{damp_sig2} from MIMO AFLNFC modulate the respective steady state reference currents, I_{o1} and I_{o2}, of the two HVDC systems.

Sequential AC/DC load flow is used to initialize the system with machine G_1 taken as a swing bus.

5. Simulation results and discussion

To validate the proposed control scheme, different simulations of various contingencies are performed to evaluate the performance in the SIMULINK/SimPowerSystem. A test power system with two HVDC links is subjected to several disturbances with variation in fault location, duration, and post-fault network alterations. Three scenarios are presented here keeping in view their high severity. The system responses are shown in terms of six inter-area oscillation modes, i.e. oscillation of generators G_2 to G_6 against the reference generator G_1. In addition, the damping performance in transient and steady-state conditions is also measured through ISE, ITSE, IAE, and ITAE. In each scenario, simulations were carried out with no HVDC damping control, PID damping control, and AFLNFC for comparison to verify the effectiveness.

5.1. Scenario # 1

A 3-phase to ground fault occurs at the time $t = 1$ second at $HVDC_1$ inverter bus B_{27}. The fault is self-cleared at 1.1 s without any physical change in the network configuration. Occurrence of fault excites inter-area modes of oscillations as shown in Figure 5. It is observed that AFLNFC performance is competitive to well-tuned

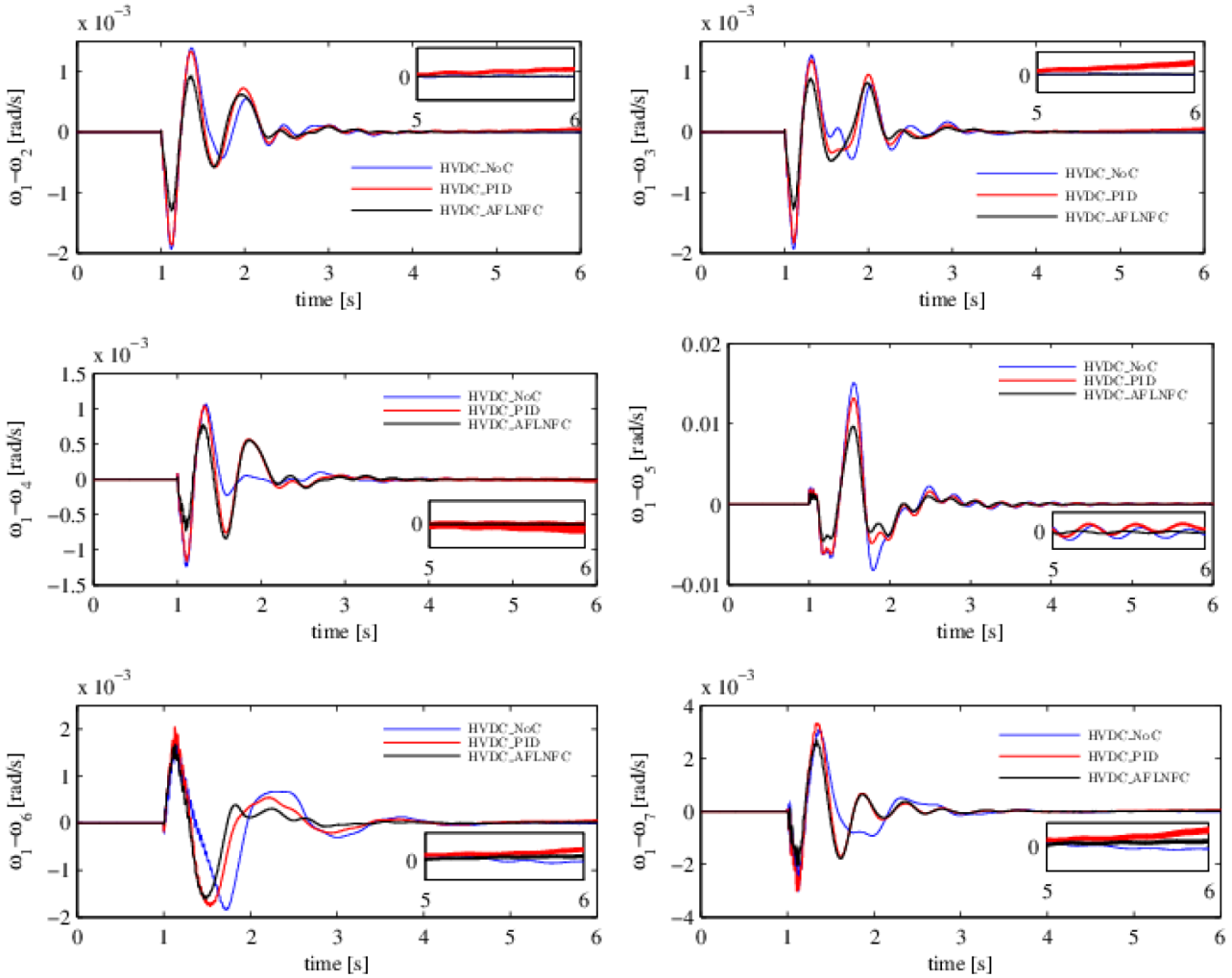

Figure 5. Relative speed deviations for various machines with fault at B_{27}.

conventional PID control and, as expected, both controllers are better than the system without supplementary control for HVDC. Performance comparison is made on the basis of overshoot and steady-state settling time. The overshoot is reduced by 18%–25% for AFLNFC as compared to conventional control and 21%–31% of the open-loop system. The LFOs decay rapidly and oscillations settle to steady-state in 3.5–4.5 s for AFLNFC unlike PID with settling time of 5–6 s. For all modes, AFLNFC completely damps LFOs with all machines gaining steady-state speed, while oscillations with small magnitude are observed from $t = 5 - 6$ s with conventional control and no control of HVDC links.

The damping assistance provided by HVDC links with AFLNFC, conventional PID control, and without control is also evaluated through performance indexes. Figure 6 shows performance indexes of error function based on speed deviation, $\sum_{i=2}^{7}(\omega_1 - \omega_i)$. The ISE plot represents a response of the system in the presence of large errors during transient state. The large oscillations decay within 3 seconds of the occurrence of fault and are represented by a flat plot for AFLNFC, PID, and no damping control of the HVDC link. However, the lower value of the AFLNFC plot reveals better performance in eliminating errors rapidly as compared to PID control. In terms of ISE value, damping is improved by 30% and 65% with AFLNFC as compared to PID and no control, respectively. The ITSE plot shows time-weighted transient-state error reduced by 30% and 71% by AFLNFC as compared to PID and no control. The IAE plot represents sustained oscillations in the system and ITAE weights errors persisting for a long time much more heavily than those at the start of the response. The ITAE index for AFLNFC shows 23% and 51% improvement in damping persistent oscillations in comparison with conventional control and no control for HVDC, respectively. As discussed earlier, there exists small oscillations with PID and no control at $t > 5$ s and the same is supported by the ITAE plot. It clearly shows a more stable AFLNFC plot as compared to plots for PID and no control, which are continuously rising.

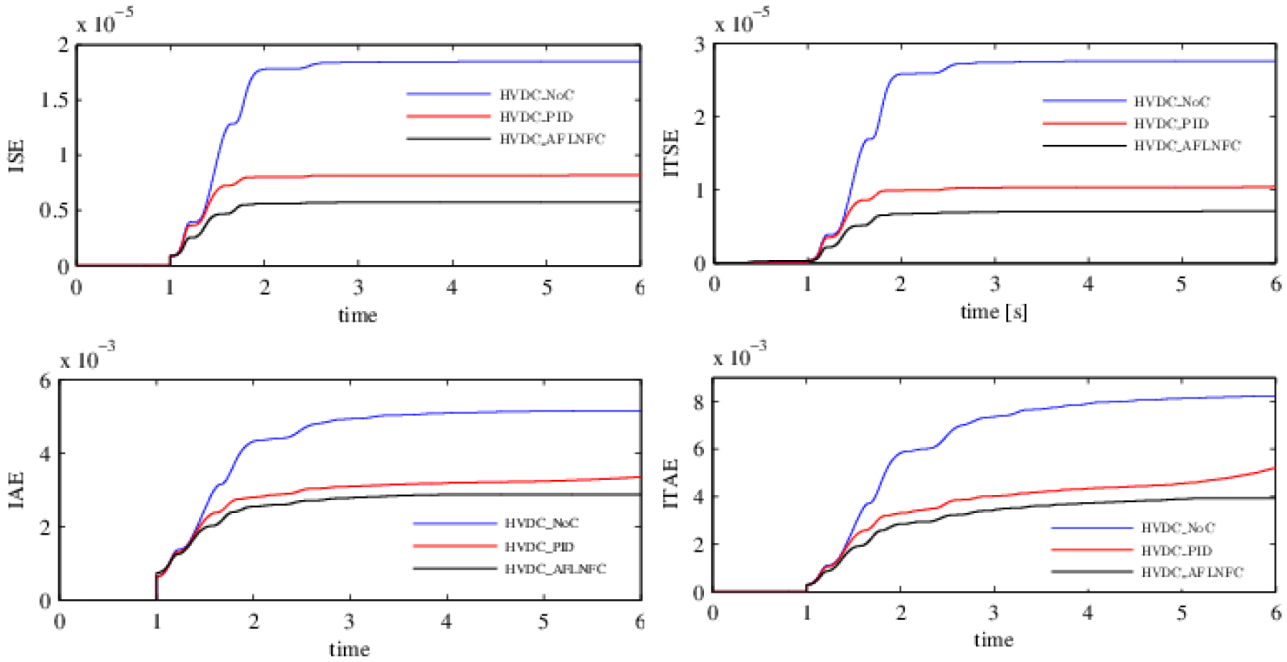

Figure 6. Performance indexes with fault at B_{27}.

Effectiveness of the proposed control strategy is also observed by the power flow through HVDC transmission systems and tie-lines between two networks as shown in Figure 7. With the occurrence of a fault,

damping signals are generated to rapidly change the power flow through the HVDC transmission system. It is observed from variations in HVDC power flows that the HVDC lines are maximally utilized by AFLNFC through modulating their real power flow. As compared to PID control and no control, AFLNFC forces HVDC lines to carry more controlled power to avoid uncontrolled power flow through parallel AC lines and dissipate energy injected into the system after perturbation. For HVDC link 1, with AFLNFC maximum power of 1560 MW has been accommodated by the HVDC system as compared to 1425 MW and 1099 MW with PID and no control, respectively. The most severe oscillations are observed in line $B_{27}B_{17}$ as it is connected to the power plant G_5, both inverters and load centers with large voltage dependent dynamic loads. However, the power flow through the tie line is more stable with AFLNFC as compared to conventional control.

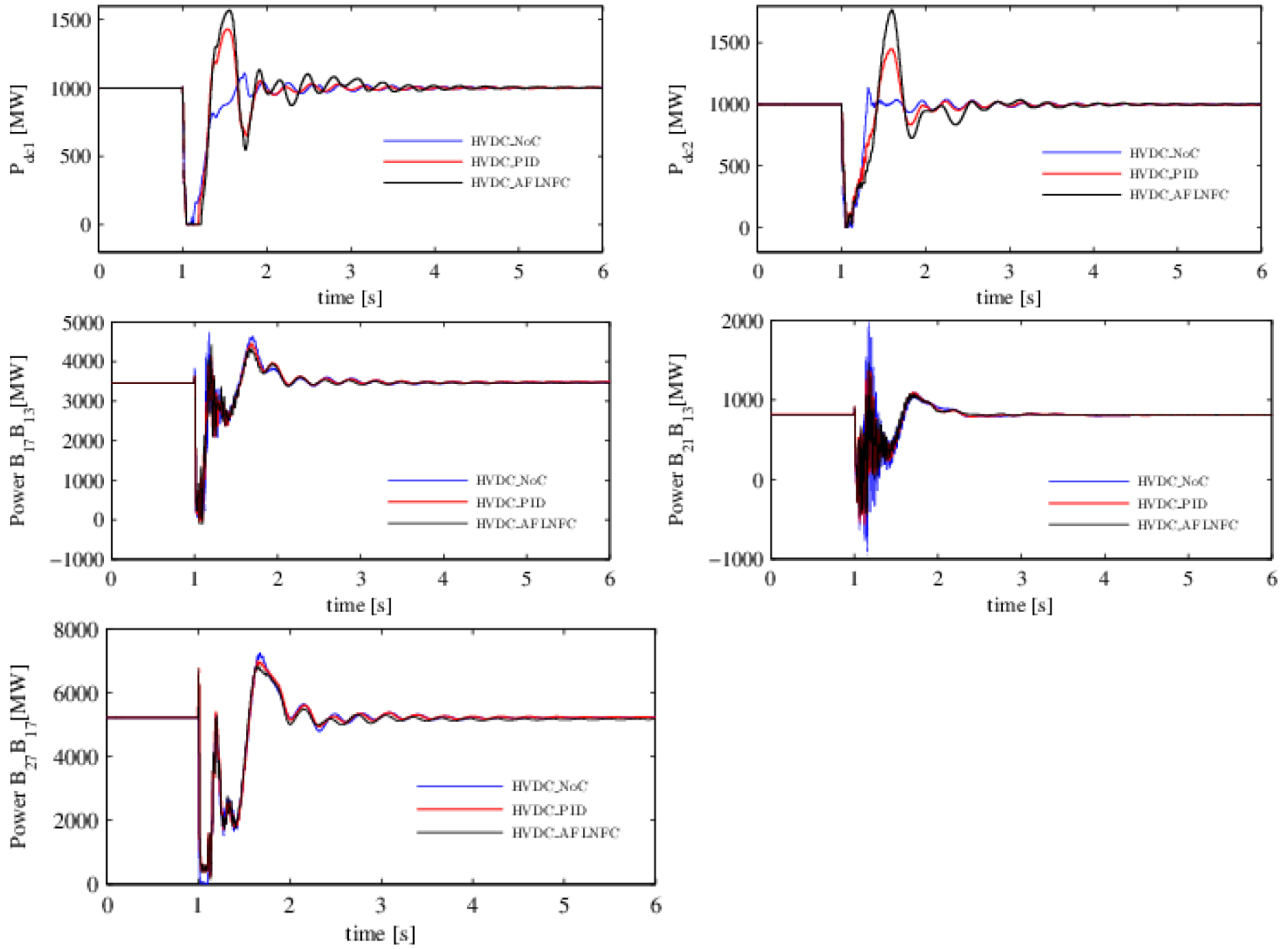

Figure 7. Power flow through HVDC and tie-lines with fault at B_{27}.

The above discussion reveals that AFLNFC has better damping performance in terms of overshoots and settling time.

5.2. Scenario # 2

To investigate the robustness of AFLNFC, the test power system is subjected to 3-phase to ground fault at the inverter bus B_{17}, at time $t = 1$ s for the duration of 6 cycles. The fault is cleared by the permanent

tripping of transmission line $B_{13}B_{17}$. Excited inter-area modes of oscillations shown in Figure 8 portray the more severe nature of disturbance as compared to scenario #1. However, AFLNFC rapidly damped-out LFOs and the system settles to steady state within 3–4 s after the perturbation has occurred while the system is still oscillating with PID and no control. With AFLNFC, the overshoots are reduced by 16%–26% and 23%–30% as compared to conventional control and open-loop systems, respectively.

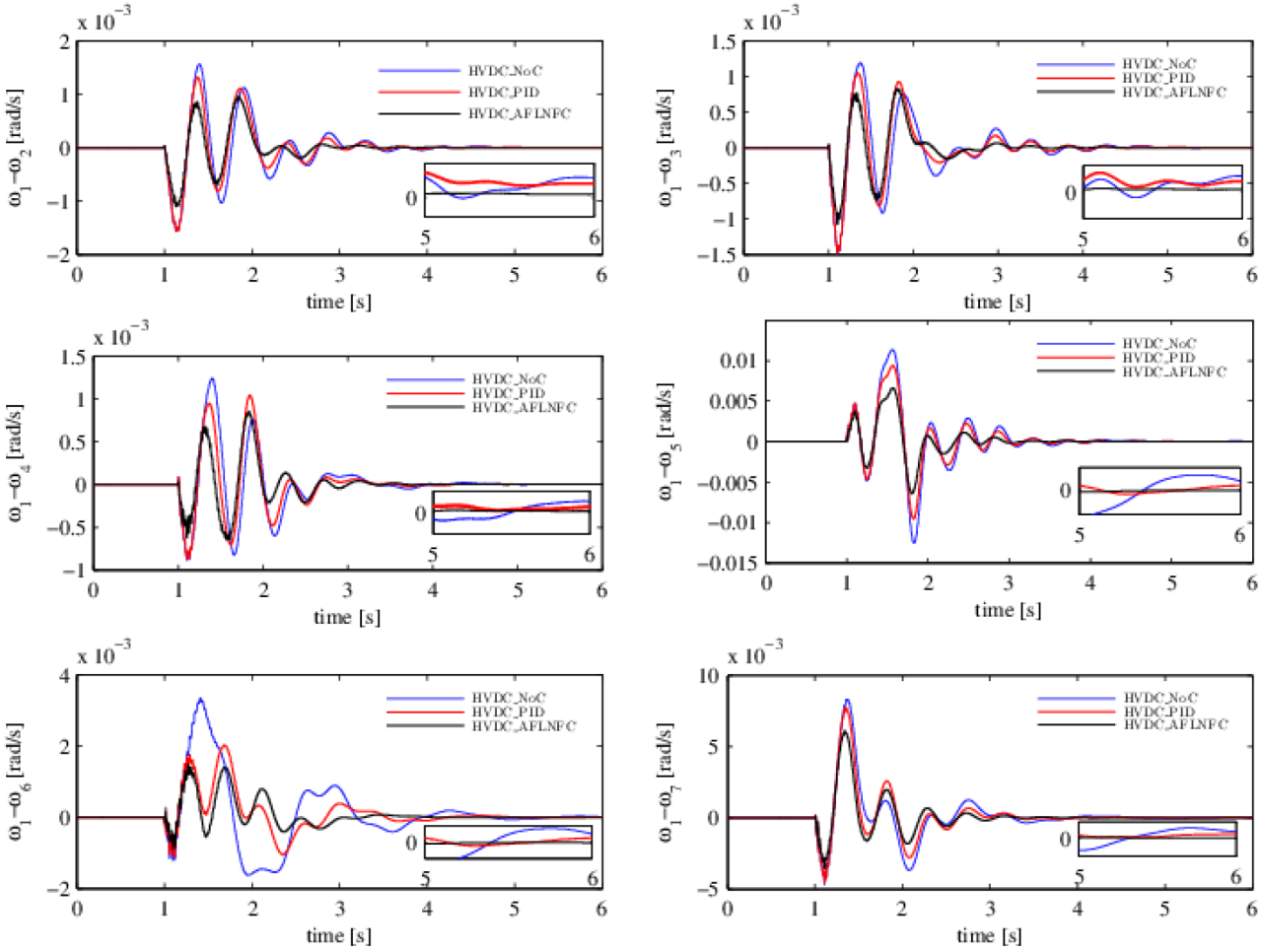

Figure 8. Relative speed deviations for various machines with fault at B_{17} and $B_{13}B_{17}$ line trip.

Performance indexes shown in Figure 9 assess the damping compensation provided by HVDC systems with AFLNFC and PID supplementary control as compared to no control. HVDC systems with MIMO AFLNFC have the least index values at any time and the flatlest profiles during steady state. ISE index shows a 30% improvement in damping transient-state oscillations as compared to conventional control and 65% over the open-loop system. Time-weighted error index ITSE for AFLNFC depicts 32% and 69% improvement as compared PID and no control. The IAE plot for AFLNFC shows 22% damping persistent oscillations while ITAE represents 28% improved steady-state stability as compared to conventional control. At $t = 6$ s, the ITAE plot with AFLNFC is more stable as compared to PID and no control that are still on the increase.

Figure 10 shows the power flow through the HVDC transmission system and tie lines between the two networks for scenario #2. With the occurrence of a fault, damping signals are generated to rapidly control the power flow through the HVDC transmission system. It is observed that AFLNFC effectively modulates the

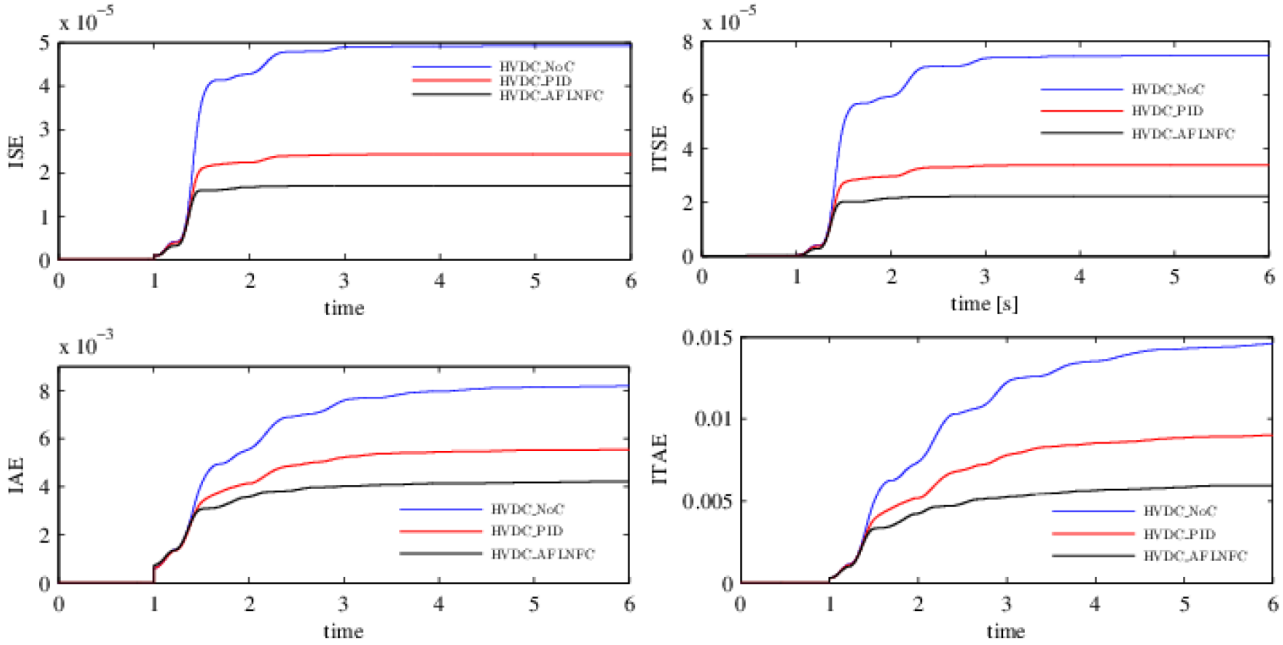

Figure 9. Performance indexes with fault at B_{17} and $B_{13}B_{17}$ line trip.

real power flow through HVDC links during transient state and offers maximum assistance in damping LFOs. During transient state, HVDC link 1 accommodates maximum power of 2414 MW with AFLNFC and 1911 MW with PID control as compared to 1152 MW in the case of no control, while HVDC link 2 accommodates 14% more power than conventional control. Rapid power change through HVDC links has reduced the stress on parallel AC lines, enabling the power system to become stable with minimum settling time. With changed post-fault network topology, tie-line $B_{21}B_{13}$ has gained new steady-state power flow of 400 MW with reversed direction, while power flow through $B_{27}B_{17}$ has reduced to 2970 MW. Power flow through tie-lines rapidly achieves new steady-state conditions with AFLNFC in comparison with PID and no control.

The above discussion affirms that AFLNFC is a more effective and robust supplementary control for the HVDC system in dealing with perturbed operating conditions.

5.3. Scenario # 3

In this scenario, the effectiveness and robust nature of the proposed control is investigated through the application of a sequence of 3-phase to ground faults. The bus B_{13} was subjected to a 100 ms 3-phase to ground fault at $t = 1$ s, followed by another fault at bus B_{22} at $t = 3.1$ s for the same duration. The response of the system is observed through inter-area modes of oscillations, performance indexes, and power flow through AC tie-lines and DC lines. Figure 11 shows the oscillatory behavior of different machines w.r.t. the reference generator. After the first perturbation, PID damping performance is competitive with AFLNFC, but it loses performance during the steady-state region after the second fault. Overshoot is reduced by 8%–16% and 14%–32% with AFLNFC as compared to PID control and no control, respectively. The second perturbation occurs while the power system is still oscillating after the first fault. After the second fault, the AFLNFC performance in terms of overshoot control is improved by 11%–17% as compared to conventional control and 18%–32% over no control. LFOs are damped-out by AFLNFC during $t = 6 - 7$ s, while PID control shows diverged behavior in most of the inter-area modes.

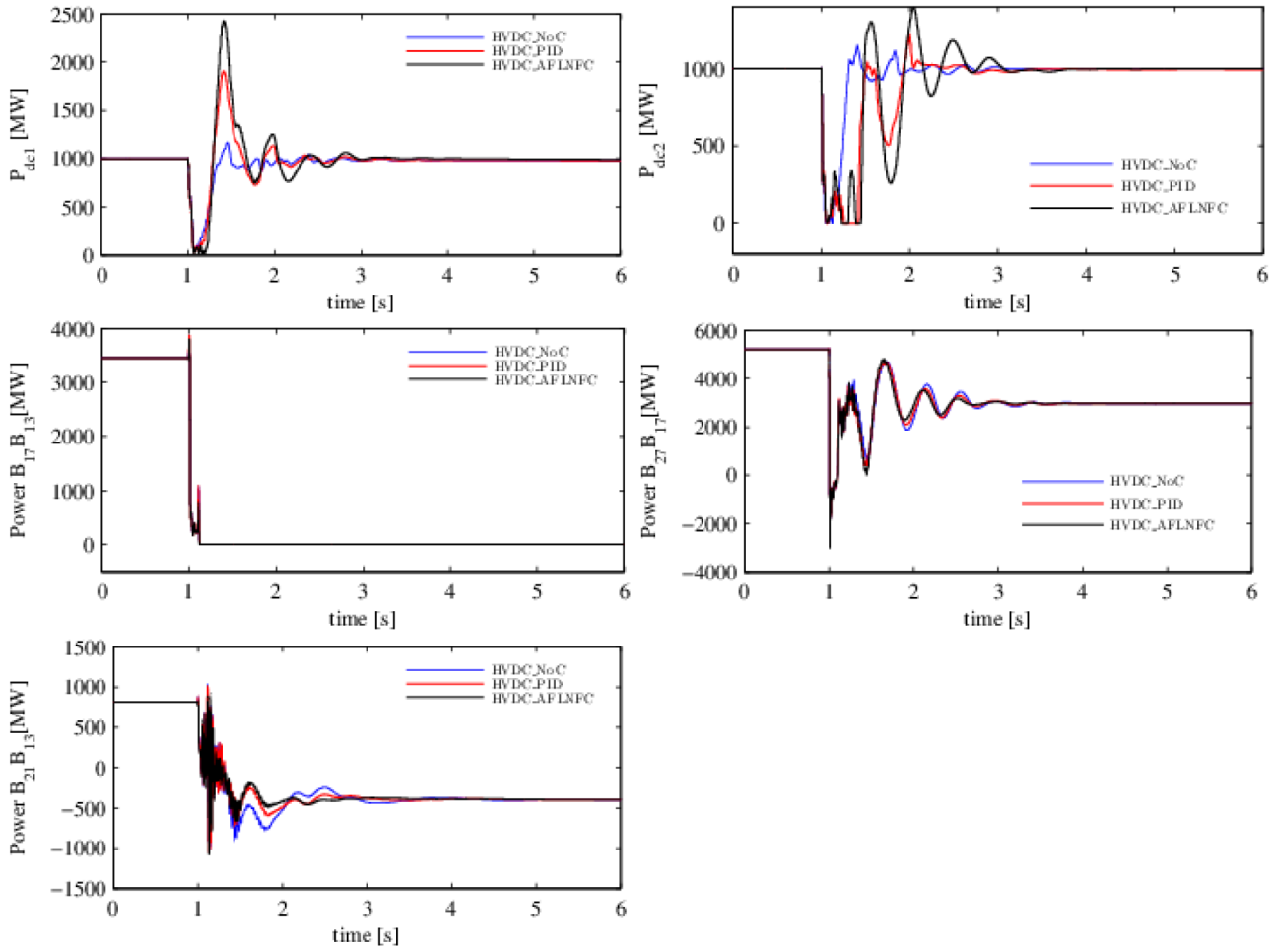

Figure 10. Power flow through HVDC and tie-lines with fault at B_{17} and $B_{13}B_{17}$ line trip.

The performance indexes shown in Figure 12 present a better picture of damping performance during transient-state and steady-state regions. As perceived by ISE and ITSE plots, transient-state errors are minimized with AFLNFC and conventional control. However, ISE and ITSE indexes for AFLNFC show an 18 % improvement in performance over conventional control with least settling time and minimized overshoots. During the steady-state region, IAE and ITAE indexes show the minimization of persistent oscillations with AFLNFC, while PID fails to cope with the situation and shows continuously growing oscillations.

Figure 13 shows the power flow through HVDC links and AC tie-lines. After the first fault, plots show 8% better modulation of both HVDC power flows by conventional control and so have competitive damping performance in comparison with AFLNFC. However, after the second fault HVDC link 1 and link 2 power flow with PID control is 11% and 19% less in comparison with AFLNFC. As compared to previous scenarios, in this case the power modulation of HVDC links during transient state is less as the fault location is far away from the HVDC system, load buses, and heavily loaded tie-lines. Moreover, AC power flow through tie-lines depicts almost the same oscillating behavior for both control strategies with less fluctuation during the transient-state region.

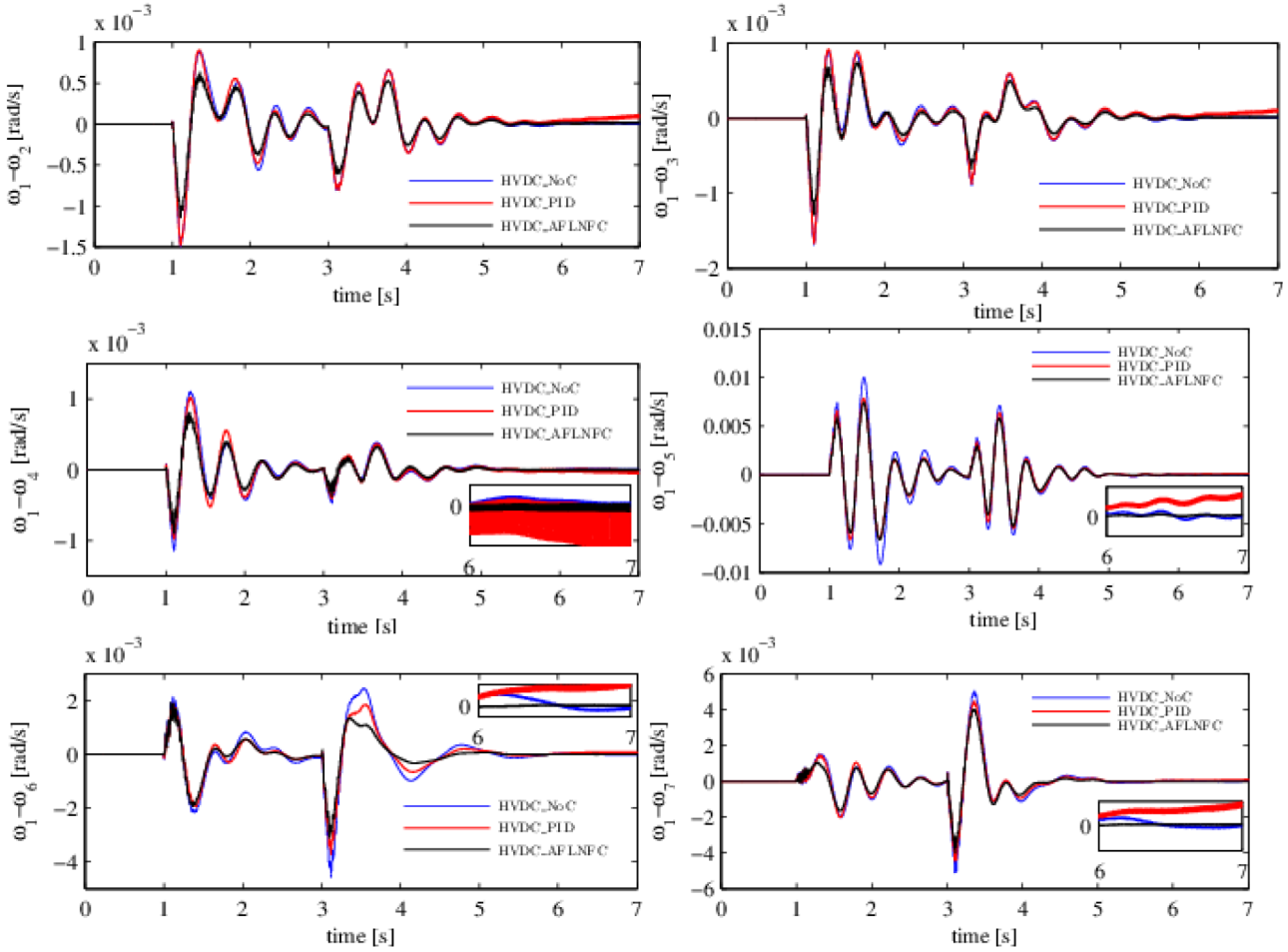

Figure 11. Relative speed deviations for various machines with sequence of faults at B_{13} and B_{22}.

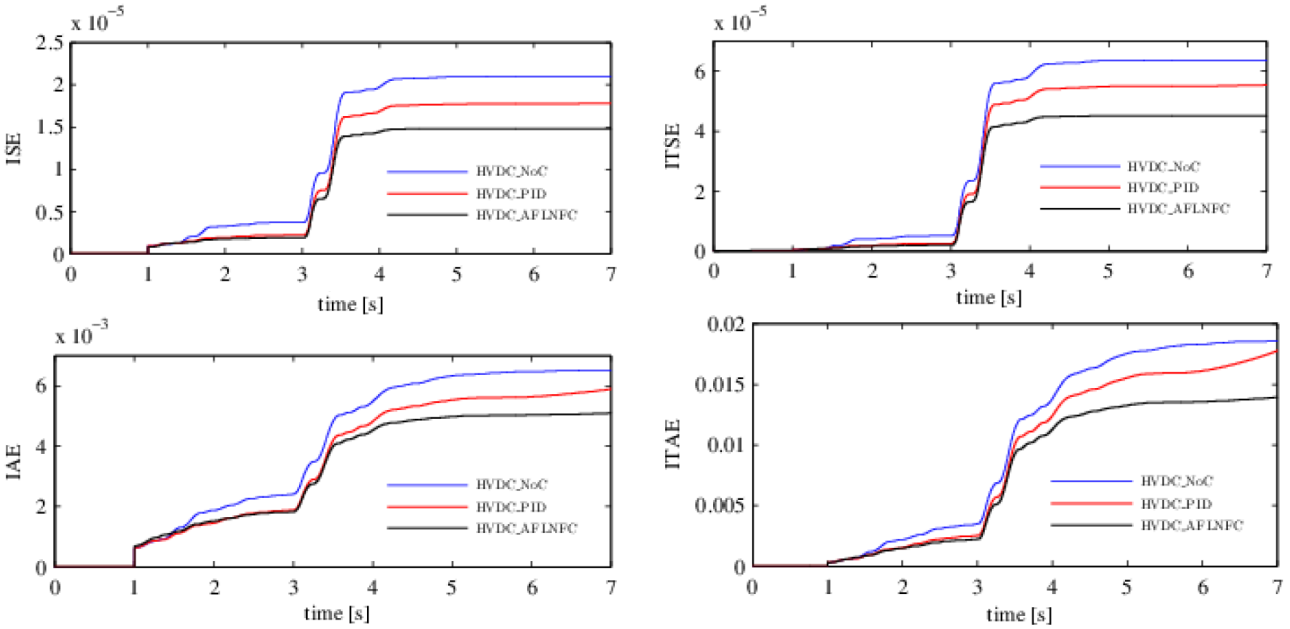

Figure 12. Performance indexes with sequence of faults at B_{13} and B_{22}.

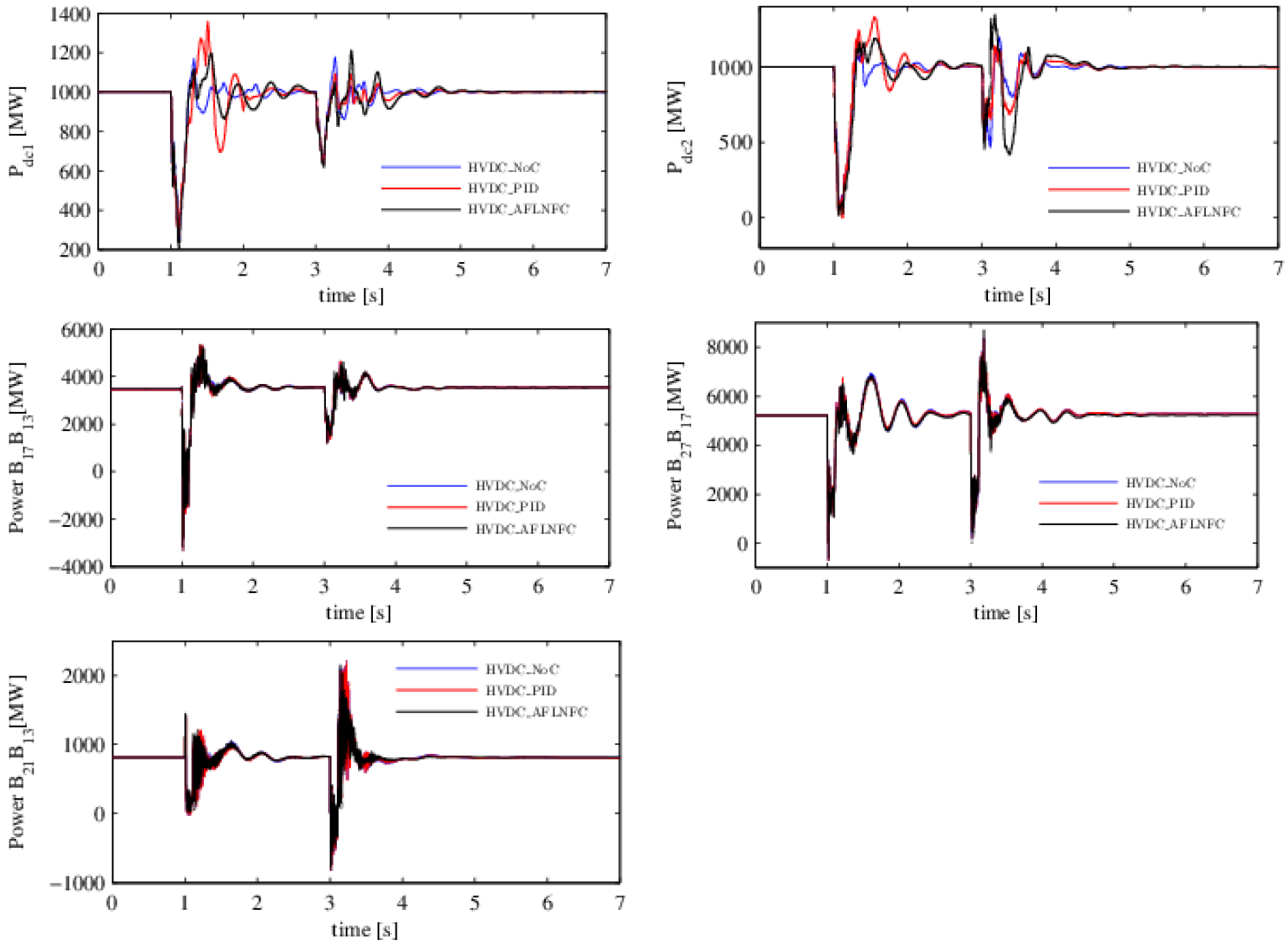

Figure 13. Power flow through HVDC and tie-lines with sequence of faults at B_{13} and B_{22}.

The above discussion of the three scenarios shows the HVDC system's capability to damp inter-area modes of oscillations with varying damping ratio. Addition of supplementary control to the HVDC system enhances its capabilities to damp LFOs during perturbed operating conditions. As compared to conventional control, the proposed AFLNFC has shown improved and robust damping performance over a wide range of operating conditions.

6. Conclusion

The article presents an online adaptive feedback linearization control strategy to design a MIMO damping controller for multiple HVDC systems to improve the stability of AC/DC power systems. The performance of the proposed AFLNFC design is ratified through the multi-machine test power system under different contingency conditions. The results are compared with conventional control to validate its performance. Online adaptive NeuroFuzzy identification empowers the rapid capturing of low frequency oscillations. The updated plant model is identified at every time step without a priori knowledge of the system model. The self-tuning capability of the proposed controller enables generation of an effective damping signal over a wide range of operating conditions. Results obtained for a wide range of operating conditions indicate that proposed AFLNFC is robust and effective in damping LFOs in a large interconnected AC/DC power system. Future work includes the incorporation of

multiple FACTS controllers to investigate their interaction with HVDC systems and the effect of damping lower frequency oscillations.

Nomenclature

V_{tR}	Rectifier pole terminal AC bus voltage
V_{tI}	Inverter pole terminal AC bus voltage
$V_{do\alpha}$	No load direct voltage of rectifier pole
$V_{do\gamma}$	No load direct voltage of inverter pole
$V_{d\alpha}$	Average direct voltage at rectifier pole
$V_{d\gamma}$	Average direct voltage at inverter pole
$I_{d\alpha}$	Rectifier pole direct current
$I_{d\gamma}$	Inverter pole direct current
α	Firing delay angle
γ	Extinction advance angle
μ	Commutation interval
a	Transformer off-nominal tap ratio
R_γ	Equivalent commutation resistance at inverter pole
R_α	Equivalent commutation resistance at rectifier pole
R_L	DC line resistance
ω_i	Speed of ith synchronous machine
ISE	Integral of the square error
IAE	Integral of absolute error
ITSE	Integral of time multiply squared error
ITAE	Integral of time multiply absolute error

References

[1] Morison K, Wang L, Kundur P. Power system security assessment. IEEE Power Energy M 2004; 2: 30-39.

[2] Kundur P. Power System Stability and Control. New York, NY, USA: McGraw-Hill Inc., 2008.

[3] Arrillaga J. High Voltage Direct Current Transmission. 2nd ed. London, UK: IET, 1998.

[4] Hammons J, Yeo RL, Gwee CL, Kacejko T PA. Enhancement of power system transient response by control of HVDC converter power. Electr Mach Pow Syst 2000; 28: 219-241.

[5] Cai H, Qu Z, Gan D. A nonlinear robust HVDC control for a parallel AC/DC power system. Comput Electr Eng 2003; 29: 135-150.

[6] Badran SM, Choudhry MA. Design of modulation controllers for AC/DC power systems. IEEE T Power Syst 1993; 8: 1490-1496.

[7] McNamara P, Negenborn RR, De Schutter B, Lightbody G. Optimal coordination of a multiple HVDC link system using centralized and distributed control. IEEE T Contr Syst T 2013; 21: 302-314.

[8] Preece R, Milanovic JV, Almutairi AM, Marjanovic O. Damping of inter-area oscillations in mixed AC/DC networks using WAMS based supplementary controller. IEEE T Power Syst 2013; 28: 1160-1169.

[9] Eriksson R, Knazkins V, Söder L. Coordinated control of multiple HVDC links using input-output exact linearization. Electr Pow Syst Res 2010; 80: 1406-1412.

[10] Khan L, Lo KL. Hybrid micro-GA based FLCs for TCSC and UPFC in a multi-machine environment. Electr Pow Syst Res 2006; 76: 832-843.

[11] Song G, Longman RW, Mukherjee R. Integrated sliding-mode adaptive-robust control. IEE P-Contr Theor Ap 1999; 146: 341-347.

[12] Marino R, Tomei P. Robust stabilization of feedback linearizable time-varying uncertain nonlinear systems. Automatica 1993; 29: 181-189.

[13] Arif J, Ray S, Chaudhuri B. MIMO feedback linearization control for power systems. Int J Elec Power 2013; 45: 87-89.

[14] Khan L, Badar R. Hybrid adaptive neuro-fuzzy B-spline based SSSC damping control paradigm using online system identification. Turk J Elec Eng & Comp Sci 2015; 23: 395-420.

[15] Khan L, Ahmed N, Lozano C. GA neuro-fuzzy damping control system for UPFC to enhance power system transient stability. In: IEEE International Multi Topic Conference; 8–9 December 2003: Islamabad, Pakistan: IEEE. pp. 276-282.

[16] Badar R, Khan L. Hybrid neuro-fuzzy Legendre-based adaptive control algorithm for static synchronous series compensator. Electr Pow Compo Sys 2013; 41: 845-867.

[17] Liang NY, Huang GB, Saratchandran P, Sundararajan N. A fast and accurate online sequential learning algorithm for feedforward networks. IEEE T Neural Networ 2006; 17: 1411-1423.

[18] Sauer PW, Pai MA. Power System Dynamics and Stability. Delhi, India: Pearson Education, 1998.

[19] Preece R, Milanovic JV. Comparison of dynamic performance of meshed networks with different types of HVDC lines. In: IET AC and DC Power Transmission Conference; 19–21 Oct. 2010; London, UK: IET. pp. 1-5.

[20] Slotine JE, Li W. Applied Nonlinear Control. Upper Saddle River, NJ, USA: Prentice-Hall, 1991.

[21] Jagannathan S, Lewis FL, Vandegrift M. Feedback linearization of nonlinear systems using fuzzy logic systems. In: IEEE 1996 ISAI/IFIS Mexico-USA Collaboration in Intelligent Systems Technologies Conference; 12–15 November 1996; Cancun, Mexico: IEEE. pp. 378-385.

[22] Nocedal J, Wright SJ. Numerical Optimization. 2nd ed. New York, NY, USA: Springer, 2006.

[23] Hager W, Zhang H. A new conjugate gradient method with guaranteed descent and an efficient line search. Siam J Optimiz 2005; 161: 170-192.

[24] Zaman H. Nonlinear self-tuning damping control paradigms for LCC-HVDC transmission system. MSc, COMSATS Institute of Information Technology, Abbottabad, Pakistan, 2013.

Appendix

- **HVDC internal control parameters** voltage base = 500 kV, current base = 4 kA

Table 1. Rectifier and inverter parameters.

Parameter	Rectifier	Inverter
Ignition angle limits, $[\alpha_{\min}\, \alpha_{\max}]$	[5° 90°]	[92° 166°]
VDCOL threshold voltage, V_{dT}	0.6 pu	0.6 pu
VDCOL minimum voltage, V_{dmin}	0.18 pu	0.18 pu
VDCOL minimum current, I_{dmin}	0.30 pu	0.30 pu
Current controller gains, $[K_p\, K_i]$	[45 4500]	[45 4500]
Voltage controller gains, $[K_p\, K_1]$	-	[35 2250]
Gamma controller gains, $[K_p\, K_1]$	-	[2 4]
Reference gamma, $\gamma_\circ$	-	8°
Reference DC voltage, V_{dref}	-	1 pu

- **Synchronous machine parameters.**

Table 2. Synchronous machine ratings.

Machine	Power (MVA)	Voltage (kV)	Frequency (Hz)	Inertia coefficient (s)
G_1	6000	13.8	60	4.1
G_2	2200	13.8	60	3.2
G_3	200	13.8	60	3.2
G_4	2700	13.8	60	3.7
G_5	5000	13.8	60	3.7
G_6	5600	13.8	60	4.0
G_7	5000	13.8	60	3.7

Table 3. Synchronous machine reactance.

Machine	$X_d\,(pu)$	$X_d^{'}(pu)$	$X_d^{''}\,(pu)$	$X_q\,(pu)$	$X_q^{''}\,(pu)$	$X_{ls}\,(pu)$	$R_{ss}\,(pu)$
G_1–G_7	1.305	0.296	0.252	0.474	0.243	0.18	0.00285

Table 4. Synchronous machine time constants.

Machine	$T_d^{'}(s)$	$T_d^{"}(s)$	$T_{qo}^{"}(s)$
G_1–G_7	1.01	0.053	0.1

Table 5. DC excitation system data.

Machine	K_a	$T_a\,(s)$	$E_{fmax}\,(pu)$	$E_{fmin}\,(pu)$	K_e	$T_e\,(s)$
G_1–G_7	300	0.001	11.5	11.5	1	0